PALACKÝ UNIVERSITY OLOMOUC
FACULTY OF SCIENCE
DEPARTMENT OF OPTICS

DIPLOMA THESIS

Description of contrast mechanisms in a scanning electron microscope

Author:	**Bc. Monika Macková**
Study programme:	N0533A110040 Physics
Field of study:	Optics and Optoelectronics
Form of study:	Full-time
Supervisor:	doc. RNDr. Roman Kubínek, CSc.
Consultant:	Ing. Radovan Vašina, CSc.
Thesis submitted on:	August 2023

UNIVERZITA PALACKÉHO V OLOMOUCI
PŘÍRODOVĚDECKÁ FAKULTA
KATEDRA OPTIKY

DIPLOMOVÁ PRÁCE

Popis mechanismů kontrastu ve skenovacím elektronovém mikroskopu

Vypracovala:	**Bc. Monika Macková**
Studijní program:	N0533A110040 Fyzika
Studijní obor:	Optika a Optoelektronika
Forma studia:	Prezenční
Vedoucí diplomové práce:	doc. RNDr. Roman Kubínek, CSc.
Konzultant:	Ing. Radovan Vašina, CSc.
Termín odevzdání práce:	srpen 2023

Abstract

Examining, describing, and simulating contrast as it occurs in a scanning electron microscope is the goal of this study. Casino software models the electron-sample interactions by generating electron paths using the Monte Carlo approach. Different materials are compared and topographic contrast is addressed by simulating various tilt angles of the sample. From the generated trajectories, backscattered electrons were selected and their spatial distribution was visualized in a form of a 3D histogram together with average energy in azimuth angles divided into bins. Further, the output was filtered by detector acceptance, which is highly dependent on the setting of the microscope. Based on the results, an artificial image was generated and compared to the images obtained using a scanning electron microscope thanks to cooperation with Thermo Fisher Scientific company. Firstly, a set of single-element samples was used to describe the decrease in intensity depending on atomic number. Then images of tin balls sample were acquired and their intensity profile was compared to the simulated one. In the future, the study could be used as a tool to recreate microscope images with any defined setting of the microscope and any sample.

Declaration

I hereby declare that I have written this Diploma Thesis and performed all the presented research and experimental tasks by myself, while being supervised by doc. RNDr. Roman Kubínek, CSc. and Ing. Radovan Vašina, CSc. I also state that every resource used is properly cited. I agree with the Thesis being used for teaching purposes and being made available at the website of the Department of Optics.

Signed in Olomouc on . . . .

. . . .
Bc. Monika Macková

Contents

Introduction

Electron microscopy was invented as a way to achieve higher resolution then optical microscopes are able to provide [1]. Electron microscopy has led to many discoveries in various fields such as microbiology [2], biomedical science [3], and chemistry [4]. By examining the nanoscale structures of materials, sensors, and devices, we may now construct new or improved materials and technologies [5].

To evaluate the image of the observed structures correctly, it is necessary to know mechanisms of image formation and emergence of contrast. Although in practice the issue is often simplified, many mechanisms and variables contribute to the creation of contrast, and it is often not easy to estimate what makes the difference in contrast between images from different detectors and what it says about the sample [6]. As the only carrier of information when detecting electrons in electron microscopy is intensity, it is crucial for even a common microscope user to understand how the electron beam interacts with the sample and which portion of the signal is captured by the detectors.

The purpose of this work is not only to describe contrast formation and electron-matter interactions, but also to model these processes thoroughly. Simulation of all the relevant mechanisms may provide better insight and possibility to exploit instrument capabilities up to its limits. Such holistic approach is probably an unique way if one wants to predict behavior of a scanning electron microscope within the vast operational conditions space. Production of synthetic artificial images of an arbitrary sample under certain conditions (e.g. landing energy, probe current and others) is still ahead of us. This work treats small part of the complex phenomenon of image creation in a scanning electron microscope (SEM). The ultimate long-term goal is to create a digital twin of the electron microscope. A digital twin is a digital representation of a real-world physical system that acts as the system's effectively indistinguishable digital counterpart for tasks including simulation, monitoring, testing, integration, and maintenance. The first block of this effort would be describing the incident beam by performing ray tracing in the electromagnetic field created by the lens system in the column. Then the beam-sample interaction needs to be simulated. This thesis will be focused on a specific type of signal electrons, namely backscattered electrons. Secondary electrons are also a significant part of the signal, but in their case, a large number of other effects such as contamination of the sample and charging would have to be considered. Investigation of all phenomena connected to emission of secondary electrons exceeds the scope of this diploma thesis. The last block involves determining the detector response, acceptance and filtering resulting signals based on that.

Electron microscopes use a beam of accelerated electrons to display the sample. The electron beam is shaped by electromagnetic fields in a microscope column. Electrostatic and magnetostatic lenses produce electromagnetic fields. With these fields, the

beam is focused and manipulated on the sample [7]. The SEM belongs to rather broad family of scanning probe instruments. A beam of particles interacts with a sample producing certain signals. Signals are collected by suitable (mostly integral) detectors and their characteristics, mostly their magnitude is visualized on the computer screen in a raster as the beam scans the specimen [8].

Signal electrons mostly consist of backscattered electrons (BSE) and secondary electrons (SE). Each is formed on the basis of a different principle, and therefore they have different characteristics, such as energy, spatial and angular distribution. They also carry different information. Backscattered electrons are formed when primary electrons collide with sample atoms and their path leads back to the surface of the sample. Their energy is often close to that one of primary electrons and their incidence is determined by the atomic number Z [9]. This dependence is the reason why BSEs are the carrier of material contrast. Secondary electrons are generated on the sample's surface or near-surface regions. They have less energy than backscattered electrons and are extremely useful for inspecting the topography of the sample's surface [10].

The topic of chapter 1 will be electromagnetic field in general and electron trajectory description, in chapter 2 the optics of primary beam and signal electrons will be addressed. Material and topographic contrast will be addressed throughout the whole work and characteristics of signal electrons will be discussed in more detail in chapter 3. In chapter 4, the results of BSE emissivity simulations based on Monte Carlo method will be presented, the data obtained by measuring on a Thermo Fisher Scientific SEM will be shown in chapter 5 and chapter 6 will be dedicated to the comparison of simulation and experiment results. The conclusion summarizes results of this diploma thesis.

Chapter 1

Electron optics

1.1 Electromagnetic field

To describe forming of the beam and tracing, it is necessary to start from the basics of electromagnetism. Coulomb's law is a fundamental physical law describing the forces that act between electrically charged particles. French physicist Charles-Augustin de Coulomb published it in 1785, laying the foundations of electrostatics. The law states that the magnitude of the electrostatic force F of attraction or repulsion between two point charges q_1 and q_2 is directly proportional to the product of the magnitudes of the charges and inversely proportional to the square of the distance r between them. The electric force between charged bodies at rest is conventionally called the electrostatic force or the Coulomb force and can be written as a vector this way

$$\boldsymbol{F}_{12} = \frac{q_1 q_2}{4\pi\epsilon_0} \frac{\boldsymbol{r}_{12}}{r_{12}^3} = -\boldsymbol{F}_{21}, \tag{1.1}$$

where ϵ_0 is the permittivity of vacuum and the directions of the vector are depicted in Figure 1.1. If we remove one charge, the Coulomb force disappears, but the possibility of a force effect on any charge that we insert into the space does not disappear. The ability to exert force on charge q is described by the intensity of the electric field $\boldsymbol{E}$ in the form

$$\boldsymbol{E} = \frac{\boldsymbol{F}}{q}. \tag{1.2}$$

The density of field lines can be used to determine the magnitude of the field strength in a certain part of space. The field lines emanate from positive electric charges and go towards negative electric charges, and they can also start or end at infinity. Field lines do not cross each other and they do not form or disappear in a space containing no free charge. The field line equation is then described as

$$\frac{\mathrm{d}x}{E_x} = \frac{\mathrm{d}y}{E_y} = \frac{\mathrm{d}z}{E_z}. \tag{1.3}$$

Gauss's law can be expressed in the following formulation:

$$\phi_E = \frac{q}{\epsilon_0}. \tag{1.4}$$

The flow of electric intensity ϕ_E through any closed surface (Gaussian surface) is directly proportional to the electric charge q located inside this surface. The proportionality constant is the inverse of the vacuum permittivity ϵ_0 [11]. The stated statement
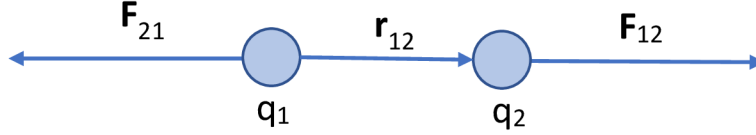
Figure 1.1: Demonstration of Coulomb's law.

is usually written in integral mathematical form as

$$\oint_S \boldsymbol{E} \cdot \mathrm{d}\boldsymbol{S} = \frac{q}{\epsilon_0}. \tag{1.5}$$

This expression of Gauss's law is also referred to as Gauss's law of electrostatics in integral form. If we consider a continuous charge distribution and express the integral in terms of volume instead of area, we get

$$\mathrm{div}\boldsymbol{D} = \rho, \tag{1.6}$$

where $\boldsymbol{D} = \epsilon_0 \boldsymbol{E}$ is electrical induction. Equation 1.6 represents one of Maxwell's equations. The intensity of the electric field $\boldsymbol{E}$ also depends on the electrostatic potential ϕ by relation

$$\boldsymbol{E} = -\mathrm{grad}\phi. \tag{1.7}$$

This part was about the electric field in a vacuum, and the following will be a basic description of the magnetic field in a vacuum. Magnetic induction $\boldsymbol{B}$ is a vector physical quantity that expresses the force effects of a magnetic field on a moving particle with a charge or magnetic dipole moment. It is the main quantity used to quantitatively describe the magnetic field. The magnetic force $\boldsymbol{F}_M$ acting on freely propagating charges q moving at speed $\boldsymbol{v}$ can be described as

$$\boldsymbol{F}_M = q(\boldsymbol{v} \times \boldsymbol{B}). \tag{1.8}$$

Fleming's left-hand rule helps us determine the relative directions of individual vectors. The force is always perpendicular to the plane created by the vector of force and magnetic induction, and its magnitude is determined by

$$F_M = qBv\sin\alpha, \tag{1.9}$$

where α is the angle between $\boldsymbol{B}$ and $\boldsymbol{v}$. Similar to electric intensity, we can define the magnetic scalar potential ψ that satisfies

$$\boldsymbol{B} = -\mathrm{grad}\psi. \tag{1.10}$$

We can also describe magnetic flux as

$$\phi_M = \oint_S \boldsymbol{B} \cdot \mathrm{d}\boldsymbol{S} = 0. \tag{1.11}$$

This relation is one of Maxwell equations in integral form and it shows that the magnetic field is non-source and thus the induction lines are always closed loops. The other

two of Maxwell's equations, which have not yet been mentioned here, no longer point to the electric and magnetic fields separately, but describe their mutual relationship. According to the Maxwell-Faraday equation, a spatially variable, non-conservative electric field is always accompanied by a time-varying magnetic field, and vice versa. The Maxwell-Faraday formula is

$$\mathrm{rot}\boldsymbol{E} = -\frac{\partial \boldsymbol{B}}{\partial t}. \tag{1.12}$$

Ampere's law relates magnetic intensity $\boldsymbol{H} = \dfrac{\boldsymbol{B}}{\mu_0}$ and electrical induction $\boldsymbol{D}$

$$\mathrm{rot}\boldsymbol{H} = \boldsymbol{j} + \frac{\partial \boldsymbol{D}}{\partial t}, \tag{1.13}$$

where $\boldsymbol{j}$ is the current density. Electromagnetic interaction is one of the basic interactions, its mediating particle is the photon. It is classified as a long-range interaction. More generally, the connection between the two fields is described by the special theory of relativity, which describes both fields using one four-dimensional antisymmetric electromagnetic field tensor, where the electromagnetic field is described by six numerical values at each point [12].

For a complete description of the electromagnetic field, we need to know the spatial distribution of $\boldsymbol{E}$ to describe the electric part of the field and $\boldsymbol{B}$ to describe the magnetic. In the case of an environment where the field is complex, for example where there are multiple electromagnetic field sources and we want to take into account the real properties of materials and calculate uncertainties, we need to use numerical methods to describe the field. An analytical solution is often impossible to obtain.

1.2 Electron trajectory

The movement of electrons in an electromagnetic field is described by the Lorentz force which combines forces described in Equation 1.2 and Equation 1.9

$$\boldsymbol{F} = -e(\boldsymbol{E} + \boldsymbol{v} \times \boldsymbol{B}), \tag{1.14}$$

where e is the charge of an electron and $\boldsymbol{v}$ represents the velocity of the electron and the direction of this vector determines the direction of motion. Based on this equation, we are able to determine how the components affect individual electrons and by extension the electron beam. We are also able to determine that the electrons travel along spiral trajectories when they are affected by magnetic field [13]. However, as mentioned in the previous section, we describe $\boldsymbol{E}$ and $\boldsymbol{B}$ numerically when we determine the path of electrons in an electron microscope column.

Newton's second law of motion states that when a body is acted upon by a force, the time rate of change of its momentum equals the force [14], which can be written as

$$\boldsymbol{F} = m\boldsymbol{a} = m\frac{\mathrm{d}\boldsymbol{v}}{\mathrm{d}t} = m\frac{\mathrm{d}^2\boldsymbol{r}}{\mathrm{d}t^2}, \tag{1.15}$$

where $\boldsymbol{r}$ represents a position vector. This equation is the basis for tracing because it allows us to determine the position using the force acting on the particle. After relativistic correction and substitution, we obtain

$$\frac{\mathrm{d}}{\mathrm{d}t}\left(\frac{m_0\boldsymbol{v}}{\sqrt{1 - v^2/c^2}}\right) = -e(\boldsymbol{E} + \boldsymbol{v} \times \boldsymbol{B}), \tag{1.16}$$

where m_0 is the invariant mass of the electron. In practical solutions, we often apply the paraxial approximation, which means that we only consider rays propagating with only small angular deviations and small distances from the optical axis.

In the case of a more complex field, a solution to the Laplace equation is sought. The partial differential equation is of the second-order linear elliptic type. Laplace equation is based on Equation 1.7 and Equation 1.10. After applying

$$-\mathrm{grad}(\epsilon\mathrm{grad}\phi) = \rho, \tag{1.17}$$

and assuming that we are in a space charge-free region, we obtain Laplace equation

$$\mathrm{grad}(\mathrm{grad}\phi) = \Delta\phi = 0, \tag{1.18}$$

The same equation applies to the magnetic equivalent ψ. We are required to employ one of the numerical analysis tools since, according to the theory of differential equations, second-order partial differential equations are typically analytically unsolvable [15]. The finite element method is the approach most frequently employed for field computations in charged particle optics (CST [16] and EOD software [17]).

To trace the electrons in the optical column, we need to find a solution to a system of differential equations. The problem can be described as

$$\frac{\mathrm{d}\boldsymbol{y}}{\mathrm{d}t} = \boldsymbol{f}(t,\boldsymbol{y}(t)), \tag{1.19}$$

where $\boldsymbol{y}$ is an unknown vector function of time t, which we would like to approximate. The known value of $\boldsymbol{y}_0$ equals to $\boldsymbol{y}$ in initial time t_0. Runge-Kutta is a group of the most frequently used iterative numerical methods for solving systems of differential equations. It is a step-by-step calculation from the initial condition. We determine the next value of $\boldsymbol{y}_{n+1}$ using the current value $\boldsymbol{y}_n$ and the weighted average of the increments $\boldsymbol{k}_i$, which contain the size of the interval h and an estimated slope specified by function $\boldsymbol{f}$ on the right-hand side of the differential equation. The equation for $n+1$ step of the explicit Runge-Kutta method has the form of

$$\boldsymbol{y}_{n+1} = \boldsymbol{y}_n + h(b_1\boldsymbol{k}_1 + b_2\boldsymbol{k}_2 + ... + b_s\boldsymbol{k}_s), \tag{1.20}$$

where increments $\boldsymbol{k}_i$ are given by

$$\begin{aligned} \boldsymbol{k}_1 &= \boldsymbol{f}(t_n,\boldsymbol{y}_n) \\ \boldsymbol{k}_2 &= \boldsymbol{f}(t_n + c_1 h,\boldsymbol{y}_n + ha_{21}\boldsymbol{k}_1) \\ &\vdots \\ \boldsymbol{k}_s &= \boldsymbol{f}(t_n + c_s h,\boldsymbol{y}_n + h(a_{s1}\boldsymbol{k}_1 + a_{s2}\boldsymbol{k}_2 + ... + a_{ss-1}\boldsymbol{k}_{s-1})), \end{aligned} \tag{1.21}$$

in which parameters b_i, c_i and a_{ij} define particular explicit Runge-Kutta method [15].

Chapter 2

Optics of a SEM

2.1 Primary beam

The primary beam optics is one of the main inputs to the image simulation. This is actually the first entry, as it precedes the part where we simulate the interaction of electrons with the sample, which will be discussed in the next chapter. The electron optics of a SEM is designed to generate a small electron probe at the specimen. The primary beam is created in the source, then guided by a system of lenses that focus the beam and apertures that cut off the highly scattered electrons and to limit aberrations. Scanning optical elements move the beam across the sample and correction components like stigmators that correct optical aberrations must also be included.

A potential difference in range between units of Volts up to tens of kiloVolts between the cathode and anode accelerates the electrons released from thermionic or field-emission sources. The landing energy and current must be variable in order for a SEM to function practically. The quantity that describes relation between current and electron-probe size is gun brightness. In thermionic emission, thermionic excitation allows electrons from the cathode material's Fermi level to overcome the work function. According to the Schottky effect, a work function decreases as the cathode's field strength increases which means that emission occurs at lower voltages. When the electric field strength (potential gradient) reaches certain levels, field emission begins. Because of these powerful fields, the potential wall in front of the cathode narrows to a few nanometers, allowing electrons from the Fermi level to pass through it via the wave-mechanical tunneling process [9].

The main two categories of sources are thermionic and field-emission. The thermionic category includes a simple source in the form of a tungsten filament heated to a temperature of 2500 K to 3000 K [18]. It consists of a V-shaped filament, a Wehnelt cylinder and an anode. A thermionic emitter with a lanthanum hexaboride crystal was another step in the development of sources as it has better properties such as higher current density, lower energy width and operates at a lower temperature than tungsten filament. Schottky emitter is formally classified as field-emission source, but it is heated to 1800 K, so it combines the principles of both categories [19]. Again we have a V-shaped tungsten wire, there is a monocrystal of tungsten with a sharp tip, further there are two electrodes suppressor and extractor. A purely field-emission source works at room temperature and is called cold field-emission gun.

Next part of the optical system is a set of condenser lenses and apertures. A condenser is an optical system of lenses that modifies electron beam current and its divergence. SEMs usually have two condenser lenses and each of them may create a crossover. The condenser decreases the electron beam current by several orders of magnitude and assures beam passage through a realistically assembled column. The task of the apertures is to limit the peripheral parts of the beam that were affected by optical aberrations or were scattered by reflections in parts of a microscope. Apertures are effective in limiting spherical aberration, stigmators are added to correct astigmatism. They must have at least four poles to produce a quadrupole field [20]. However, hexapole, octopole, and decapole stigmators are also employed for advanced aberration corrections. Then there is a final lens that focuses the beam on the sample and therefore creates a probe. Of all lenses, the quality of the final lens matters the most, as imperfections in the final lens contribute the most to aberrations. In Figure 2.1, we can see a scheme of the electron-optical column with the condenser system and final lens. This scheme is valid only in the case of thermionic emission as we are trying to demagnify the source as much as possible. Lenses are divided into electrostatic and magnetic. The electrostatic lens consists of two or more electrodes at different potentials, and the electromagnetic one consists of a solenoid coil embedded in a ferromagnet. They produce a field of electric intensity in the case of an electrostatic lens and a magnetic induction in the case of a magnetic lens [21].

Of the optical defects, spherical and chromatic aberration and astigmatism are most commonly dealt with in electron microscopy. In case of off-axis aberrations, we often encounter coma as well. Spherical aberration causes rays incident on an electron lens focus closer to the lens if they are further from the optic axis than those that are near the axis. Chromatic aberration occurs because the electrons from the gun have an energy spread and the focal length depends on the electron energy. To explain astigmatism, the following coordinate system will be introduced. The beam propagates along the z-axis and its cross-section is defined on the x- and y-axes. Astigmatism manifests itself so that the beam is focused for the x-axis at a different distance z than for the y-axis. In the x-y plane the beam has a shape of an ellipse. In an optical system, the term coma refers to an aberration that causes off-axis point sources to seem deformed and give the impression of having a comet-like tail. Coma is defined specifically as a change in magnification over the entrance pupil. Along with diffraction, chromatic aberration, spherical axial aberration, and finite size of the electron source are the reasons why the beam is focused into a disc and not a single infinitely small point. For an aberration-free system, the source would be projected as the Airy disk due to diffraction. The disks half-width is given by the equation

$$d_d = 0.61 \frac{\lambda}{\text{NA}}, \tag{2.1}$$

where NA is numerical aperture, which is given by sine of the semi-angle. This relation describes the diffraction on the final lens and is also known as the diffraction limit of resolution. The diameter of the beam trace d is denoted as the instrument resolution and it is formed, together with d_d, by the size of the reduced crossover d_g and the contributions of spherical d_s and chromatic aberrations d_c. The size of the reduced crossover d_g an be easily expressed as the source tip diameter d_0 multiplied by its demagnification M
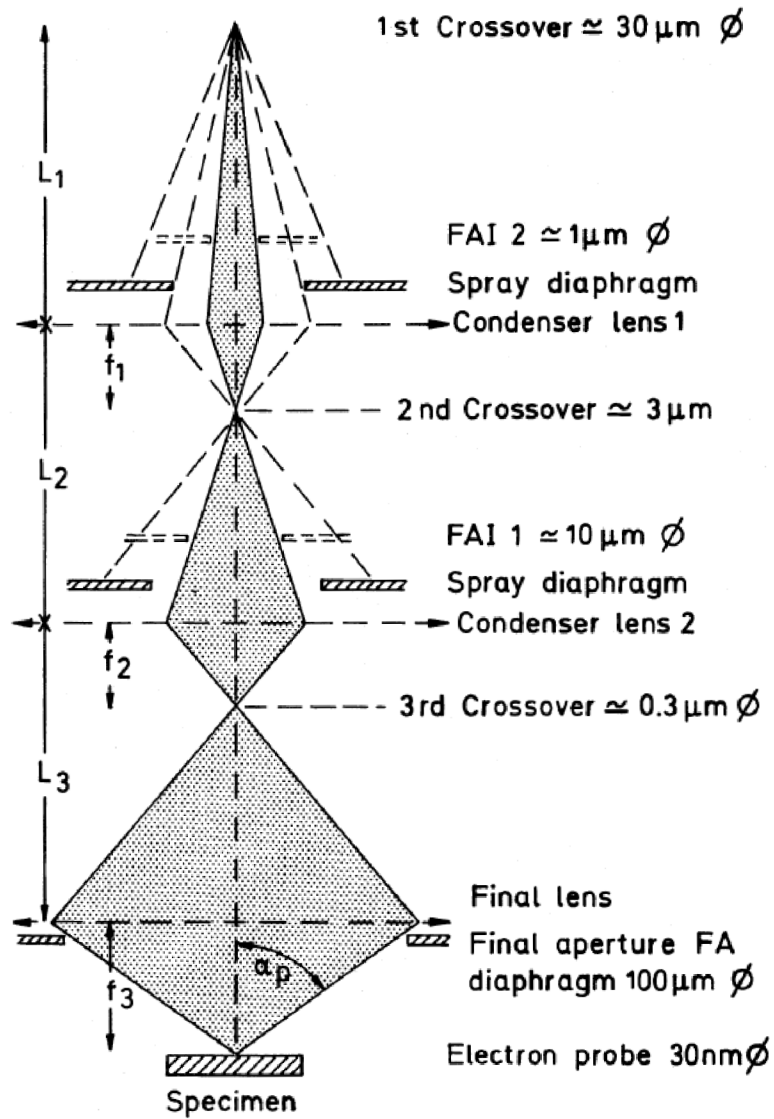
$$d_g = d_0 M. \tag{2.2}$$

1st Crossover $\simeq 30\,\mu m\ \emptyset$

L_1

FAI 2 $\simeq 1\mu m\ \emptyset$
Spray diaphragm
Condenser lens 1

f_1

2nd Crossover $\simeq 3\,\mu m$

L_2

FAI 1 $\simeq 10\,\mu m\ \emptyset$
Spray diaphragm
Condenser lens 2

f_2

3rd Crossover $\simeq 0.3\,\mu m\ \emptyset$

L_3

Final lens
Final aperture FA
diaphragm 100$\mu m\ \emptyset$

α_p

f_3

Electron probe 30nm$\emptyset$

Specimen

Figure 2.1: Schematic depiction of the electron-optical column of a SEM with an emitter based on thermionic emission [9].

The contributions d_s and d_c are dependent on aperture angle α and aberration coefficients C_s and C_c according to equations

$$d_s = 0.5 C_s \alpha^3; d_c = C_c \alpha \frac{\Delta E}{E}, \tag{2.3}$$

where ΔE is the energy spread and E is the energy of primary electrons. The total d is then determined by the relation

$$d^2 = d_d^2 + d_g^2 + d_s^2 + d_c^2. \tag{2.4}$$

2.2 Optics of signal electrons

In this section, we will discuss in more detail how detection is handled in practice and which properties of the detector need to be taken into account when simulating the resulting image. The position and size of the detector will affect the resulting contrast in the image.

Overall, when detecting electrons, we most often encounter scintillators, where photons are created after the impact of electrons and then they are detected by light detection methods typically involving semiconductors. There are also detectors based on the direct detection of electrons, where there is no conversion of electrons into light. There are different aspects of the detectors: principles, their design and their optical position.

For this purpose, the location and electromagnetic field around the detectors is more important than the exact description of their construction. The fundamental difference between BSE and SE detection lies in the fact that SE electrons have a lower energy and thus their path can be more easily influenced by an electromagnetic field. BSEs are harder to influence due to higher energy, therefore it is necessary to use a large solid angle of collection. Detection close to the sample is ideal and therefore placing the detector in the lower part of the pole piece is a common solution.

An scheme of a placement of the detectors that were used in experiments on the Thermo Fisher Scientific Apreo SEM within this diploma thesis is shown in Figure 2.2. A variable parameter in SEM is also the so-called working distance, which I will later refer to as WD. This is the distance of the sample from the pole piece of a final lens. CBS and T1 are detectors designed for backscattered electrons detection. CBS is retractable and based on a detection without conversion to photons. On the other detectors, not many backscattered electrons are collected due to the small acquisition angle. To detect signal electrons in column, it is necessary to apply a positive voltage to the so-called booster tube, which is located inside the column. The functionality of booster tube is to accelerate secondary electrons and high-loss backscattered electrons so that scintillation event may be triggered. Precisely because they collect different signals, we see slightly different contrasts on each detector under the same conditions as it is shown in Figure 2.3. The sample used is by its nature topographic and composed of one material, we can see a tin ball (later referred to in Figures as TB) with a diameter around 10 μm. T1 detector, as it is placed in the lower part of the pole piece, collects BSEs and on the tin ball we can see peak intensity in the middle of the ball, then slow drop of intensity towards the fringe and near the fringe steeper drop. Intensity profile of a tin ball measured by T1 will be further examined through the rest
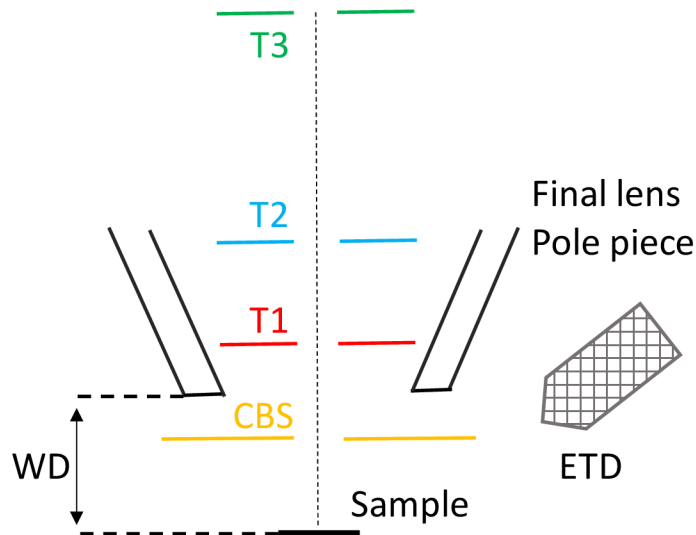
Figure 2.2: Final lens of a SEM with in-lens detectors and Everhart–Thornley detector (ETD). T1 detects BSE electrons, booster tube in the column attract SE electrons which are detected by T2 and T3 detector. CBS is a retractable detector intended for the direct detection of BSE.

of this paper. T2, T3 and Everhart–Thornley detector (ETD) are designed to collect mostly SEs and we can see that in the case of T2, T3 the image is very similar. In the middle of the ball, there is the lowest point, towards the fringe the intensity is slowly increasing and then a sharp increase on the fringe. The situation is somewhat inverse to BSE contrast. If we take look at ETD detector, we can see that on side of the ball is brighter than the other. That is of course caused by the fact that it is placed on the side and not directly above the sample. But trend of brighter edges still applies even though the edge is not as comparatively bright as it is on T2 or T3.

Detectors generally have angle- and energy-dependent acceptance. The minimum detectable electron energy is limited because it must be sufficient to excite the scintillator or to create an electron-hole pair in a PN junction. Accepted angles are determined by the already mentioned geometry of the detector, but also by the working distance. The acceptance is determined based on tracing of signal electrons which is demonstrated in Figure 2.4. It shows that lower energy electrons are affected more strongly by electromagnetic field then higher energy electrons, so their trajectory is more bent. As a higher energy example, 10 keV was used to demonstrate how BSEs behave in a field formed by the booster tube. Electrons with energy 10 eV were traced to show how secondary electrons would be affected by the field.
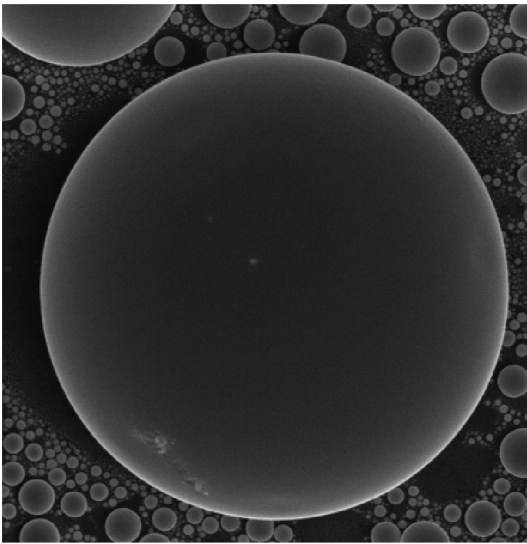
2.3   Detectors

Detectors are divided into direct ones, where the electron hits a semiconductor detector and thus contributes directly to the signal, and indirect ones, where the electron-photon conversion occurs on a scintillator and then the light is detected.
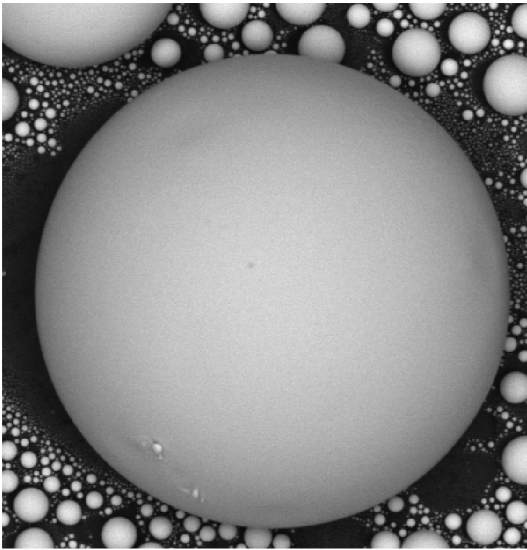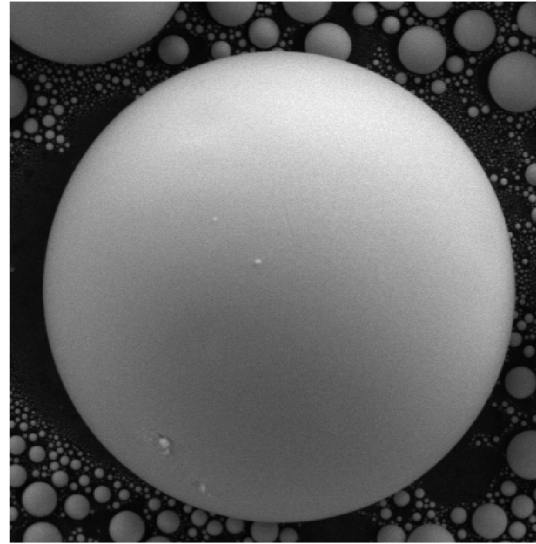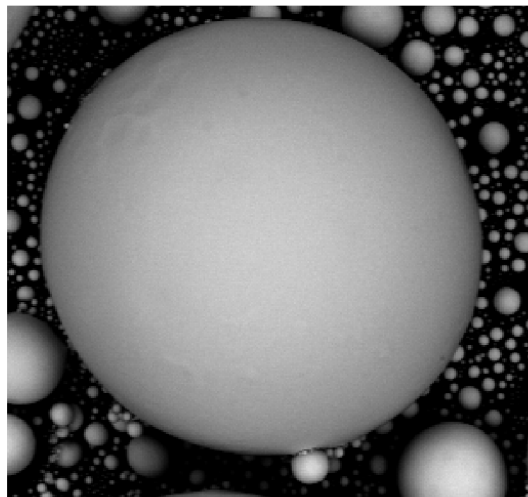
(a)
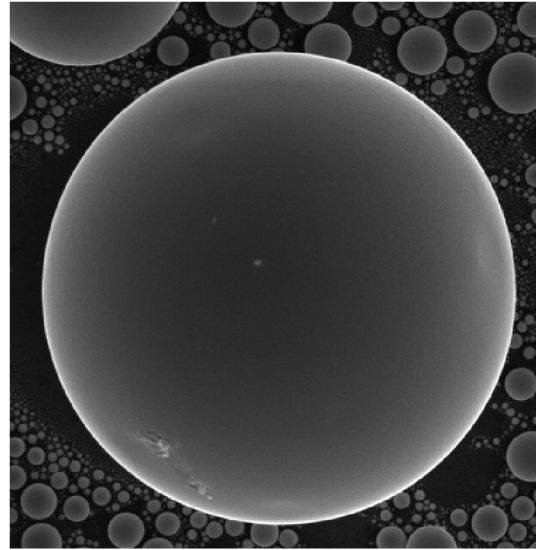
(b)

(c)

(d)

(e)

Figure 2.3: Image of a tin ball captured by a) T1, b) T2, c) T3, d) ETD and e) CBS detector. Images a)-d) were taken on Apreo SEM under these conditions: 10 kV high voltage, 10 mm working distance, booster tube 8000 V. Image e) was taken on a different microscope because it was equipped with CBS.
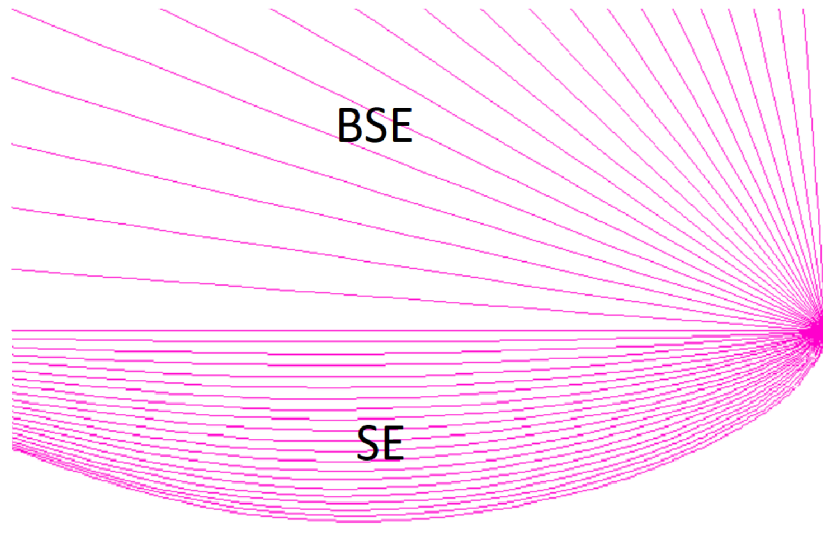
Figure 2.4: Signal electrons tracing (pink lines) performed in EOD software for electrons with 10 keV energy (upper half) and 10 eV energy (lower half). The sample is depicted in turquoise color. Working distance is 10 mm. Electrons are affected by a field formed by the booster tube which is on 8000 V.

2.3.1 Direct detection

Multi-pixel photon counter (MPPC), which is a frequently used technology in electron detection, is physically an matrix of avalanche photodiodes (APD), where one APD represents one pixel. In Figure 2.5, there is a construction of one APD depicted. The four layers of an avalanche photodiode are N, P, pure semiconductor, and P +. A protective ring formed of an N-type semiconductor surrounds the N and P layers, between which the avalanche phenomena occurs, increasing the diode's resistance to surface voltage breakdown. Charged particle passing through semiconductor causes production of electron hole pair with probability η. A powerful electric field moves the electron to the avalanche zone, where it is accelerated until it collides with the crystal lattice and creates another electron-hole pair. A powerful electric field accelerates the newly produced electron, and as it does so, more and more new electron-hole pairs are formed, producing an avalanche effect. A signal's amplification by an avalanche process occurs across a short distance—just a few micrometers—and amplifies the photocurrent by a significant factor [22]. This introduces gain G and boosts responsivity. Responsivity is the ratio of generated photocurrent and incident optical power which can be expressed as

$$R = \frac{\eta G e}{h\nu},\tag{2.5}$$

where ν is the frequency of detected light. Thickness of front implant creates a dead layer and decreases efficiency. The dead time of the detector is one the most significant parameter in detection. The detector cannot measure until the dead time has passed since it needs this time to recover from an detection event [23]. Other phenomena that occurs as well is afterpulsing. A single photon can produce many electrical pulses, which causes the incident count rate to be up to 10 % higher than it actually is and increases the dead time. It happens when charge is accumulated in the detector during dead time [24]. Additionally, false detections do occur occasionally. They are known as dark counts [25]. The amount of time needed for the detector to react to an optical
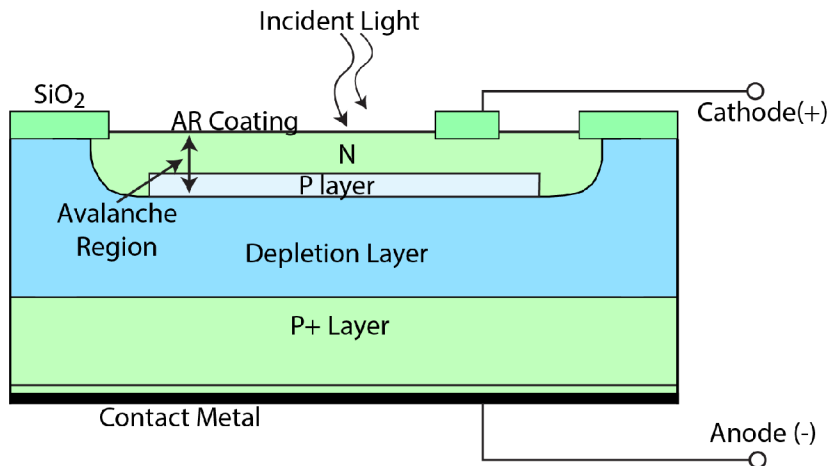
Figure 2.5: A scheme of an APD construction [26]. There are N, P, pure semiconductor, and P + layers. We can see where photon absorption occurs and where avalanche multiplication takes place.

input is known as the response time. The noise-equivalent power (NEP), which is the equivalent of the rms noise current in a 1 Hz bandwidth, is the minimal input optical power required to generate photocurrent. The I-V (current-voltage) characteristic of a diode in either forward or reverse bias (applied voltage) is described by the Shockley diode equation or diode law

$$I = I_S \left(e^{\frac{U_D}{nU_T}} - 1 \right), \tag{2.6}$$

where I is diode current, I_S reverse bias saturation current, U_D voltage across the diode, U_T thermal voltage and factor n represents a measure of ideal behavior. For ideal diode $n = 1$.

2.3.2 Indirect detection

In a scintillator, signal electrons are transformed into light, which is then transported by a lightguide to a photomultiplier, which amplifies the signal and transforms it into current. Electron energy needs to be in range of keV to produce light in scintillator. A photomultiplier is a tube with a photosensitive cathode, where an external photoelectric effect takes place, and several dynodes, where the signal is multiplied. The energy of the electron must be higher than the work function of the cathode material. The cathode efficiency is given by

$$\eta_p = (1 - R) \frac{v_e}{\alpha v_e + 1} p, \tag{2.7}$$

where R is the reflectivity of the input window, v_e is the electron escape velocity, α is the absorption coefficient and p the probability of electron excitation.

Even in indirect detection, semiconductor technology is often used. A typical detector consists of fluorescent layer on MPPC diode. After absorbing a photon in a PN junction, an electron-hole pair will form with a certain probability. This probability is called the inner quantum efficiency η. The external efficiency is then given by the reflectivity of the environment interface. The properties of semiconductor detectors
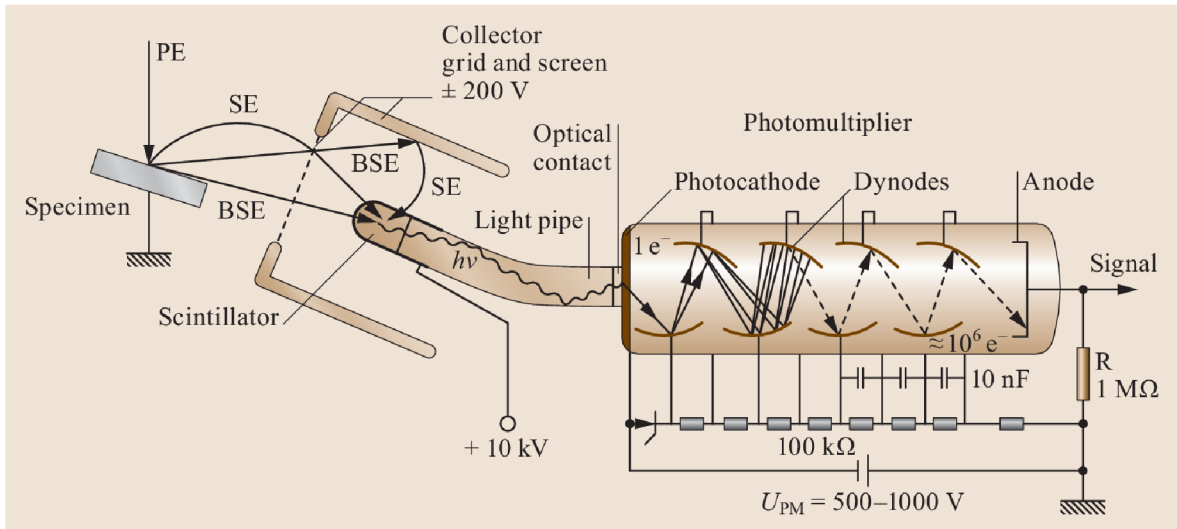
Figure 2.6: An Everhart-Thornley detector construction [27].

from the previous subsection apply here as well.

An Everhart-Thornley detector is an example of a technology employing indirect detection which is often used for secondary electrons collection. It is a positively biased grid in front of a scintillator screen which leads to photocatode and a photomultiplier as it is shown in Figure 2.6. The positive biases causes low energy electrons to be attracted to the grid. Physically, this detector is located on the side of the column tilted towards the sample.

The block after detector is called the preamplifier. There is an offset, filtering and amplification applied. The amplifier introduces gain in the range of 10 thousand to 10 million. Next step consists of current to voltage converter and differential driver that produces two outputs, one of which is inverted, and these outputs are passed to the scanning and acquisition engine. Next parts of the process will be discussed in the following sections of this chapter.

2.4   Image formation

The image is formed point by point in SEM. The detectors collect the signal from the scanning points and thus we obtain information about the intensity at individual points. So measuring with one detector we get only one number from each point. In contrast to SEM, in the transmission electron microscope (TEM) the examined area is irradiated all at once and there is no scanning. The principle is closer to classical imaging in a light microscope. One of important scanning parameters is dwell time, which is the time when the beam stays at one point on the sample. The longer this time is, the more signal is obtained, so a better signal-to-noise ratio is achieved. Scanning is always from one side to the other, then the beam returns to the original side and the next line is scanned. It does not scan in a zig zag manner, because if there was a drift, the scanned element would move to a different side each line and it would break up the image. It is possible to set line integration, which is a number that indicates how many times one line is scanned. The resulting line intensity profiles are then averaged.

Microscopes also offer a mode where acquisition is done from only one point on the sample. It is usually used to measure current at a given location.

2.5   Digital post-processing

The output signal from the preamplifier can be processed using one of three different techniques. It is the integration method, which is widely used, the simple counting method, which ensures accurate pulse counting by employing one level of discrimination, and the peak detection method, which looks for regional maxima in preamplifier output signals [28]. In the case of the integration method, the output signal is first sampled, which means that amplitudes of the preamplifier output signal are stored with a certain sampling period. It is important that the sampling is synchronized with the scanning clock. In the case of the the simple counting method, the signal pulses that cross a threshold with a rising edge are regarded as detected events if their distance from the time axis is greater than the dead time of the counter. The peak detection method is also suited for pulse counting. Only peaks with amplitude higher than the discrimination level, which is given by the parameter Level, are considered as detected events. After evaluating the signal, we divide the data into individual pixels according to the dwell time.

The resulting image frame is then passed through a static contrast/brightness block that applies a linear gain and offset to each value. In almost all cases (detector specific) the gain is set to 1.0 and offset is set to 0. At this point the data is passed to the Microscope PC (MPC) as 16 or 8 bit values. If using 8-bit values, only the most significant 8-bits are sent to the PC. The MPC captures the data and sends it through a series of buffers to form frames. There is an optional Integration/Averaging filter in the image processing pipeline that will perform integration or averaging when enabled. Finally, the images pass through a series of LUTs that are controlled by the UI digital post processing steps. The next block after scan acquisition engine is a server, where we view the image. In the server, there is a possibility to apply gamma function that transforms a linear response to a non-linear one.

Chapter 3

Electron beam and matter interaction

3.1   General remarks

When the beam of accelerated primary electrons hits the sample, elastic and inelastic scattering occurs, which results in a number of signals that are used for imaging and determination of the composition [29]. It is not a single scattering event, but rather a series of such events, when the electron gradually loses energy and possibly remains in the material and creates a charge in the sample [30] or gets out of its surface. As it was mentioned in introduction, secondary electrons and backscattered electrons mainly contribute to the formation of the image. They will be further discussed in section 3.2 and section 3.3.

Auger electrons appear with a smaller frequency than SEs and BSEs, but they are no less important as they hold a different information about the sample. The Auger electron is formed when a collision with primary electron ejects an inner-shell electron, an electron from a higher level falls into the vacancy, and a photon with energy equal to the difference between the levels is emitted. Such photons, when not absorbed, form characteristic radiation X-rays. Auger electron is an electron from outer shell that absorbs all the energy of the photon and therefore also carries information about the energy levels in an atom of the sample [31]. Both characteristic X-rays and Auger electrons are used to determine sample composition. We can also observe braking radiation (Bremmsstrahlung) as a result of electron deceleration and cathodoluminescence which causes the generation of light. A schematic overview of signal electrons and electromagnetic radiation is shown in Figure 3.1. The electrons that are absorbed into the sample form a charge that needs to be dissipated. Therefore, a conductive layer of metal is applied to the samples if they are not conductive, and the sample must be grounded [30]. In the case of transmission electron microscopes, it makes sense to talk about transmitted and diffracted electrons, whereas in a regular SEM, the signal is detected above and below the sample.

Another impactful characteristic is the depth of the sample from which the signal electrons emanate. On Figure 3.2, interaction volume is displayed and it shows that BSEs are coming from larger depth than SEs and Auger electrons. Interaction depth is important because it shows from which part of the sample we receive information. For example, we know whether we are determining the composition of only the surface or
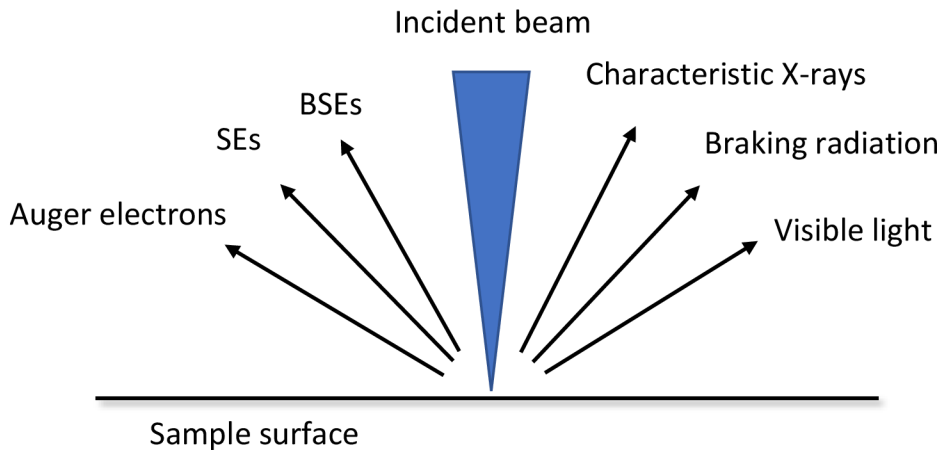
Figure 3.1: Scheme of electron beam-sample interaction. Backscattered electrons (BSE), secondary electrons (SE) and Auger electrons constitute signal electrons and there are also characteristic and braking X-rays as well as visible light caused by cathodoluminescence.

a larger sample volume, or we can decide whether it is better to detect electrons with higher or lower energy to characterize the surface tomography. The exact depths and magnitudes of the interaction volume will vary for different samples, but are approximately estimated in the caption of Figure 3.2. In order to determine the interaction volume as the radius of a hemisphere centered on the beam impact point that contain at least 95% of the trajectories, Kanaya and Okayama created a range equation that took into account both inelastic and elastic scattering

$$R_{\text{K-O}}[\text{nm}] = 27.6(A/Z^{0.89}\rho)E_0^{1.67}, \tag{3.1}$$

where A is the atomic weight in g/mol, Z is the atomic number, ρ is the density in g/cm^3 and E_0 represents the primary energy in keV [32]. Secondary and Auger electrons can only exit the specimen through a very thin surface layer that is only a few nanometers thick because they are particularly vulnerable to elastic and inelastic scattering [9]. In some circumstances, the contribution to the signal declines exponentially with increasing depth and interaction volumes might not be conclusively bordered.

Energy histogram for SEs, BSEs and Auger electron is shown in Figure 3.3. SE and BSE are distinguished by a limit given by 50 eV. In practice, we do not know which electron is SE or BSE, but if we focus on lower energies, we know we detect mostly SEs and vice versa. Another finding is that the SE and BSE spectrum is continuous, while Auger electrons create peaks in the spectrum [9]. This, of course, is due to the fact that they represent the energy of the levels in the atom, which are discrete. For conductive metals, the energy loss (plasmon) to the conduction electrons happens in discrete quanta that arise from the conduction electrons group oscillations [33].
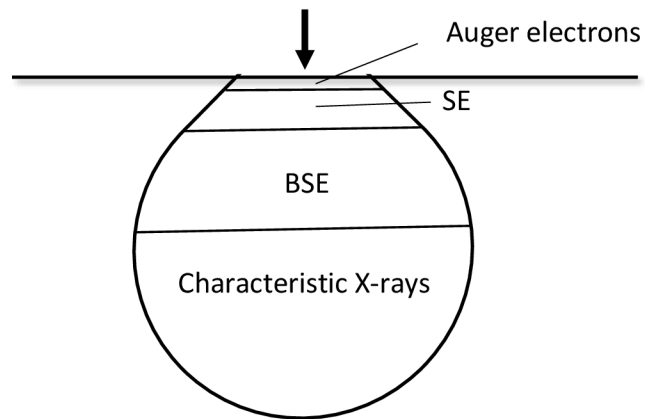
Figure 3.2: Scheme of an interaction volume. Auger electrons come from the surface of the sample (nanometers deep), secondary electrons are emitted from more depth than Auger, but still near the surface (nanometers to tens of nanometers deep) and BSE electrons are arising from about hundreds of nanometers to micrometer depth. Characteristic X-rays emanate from even deeper area of the sample [32].
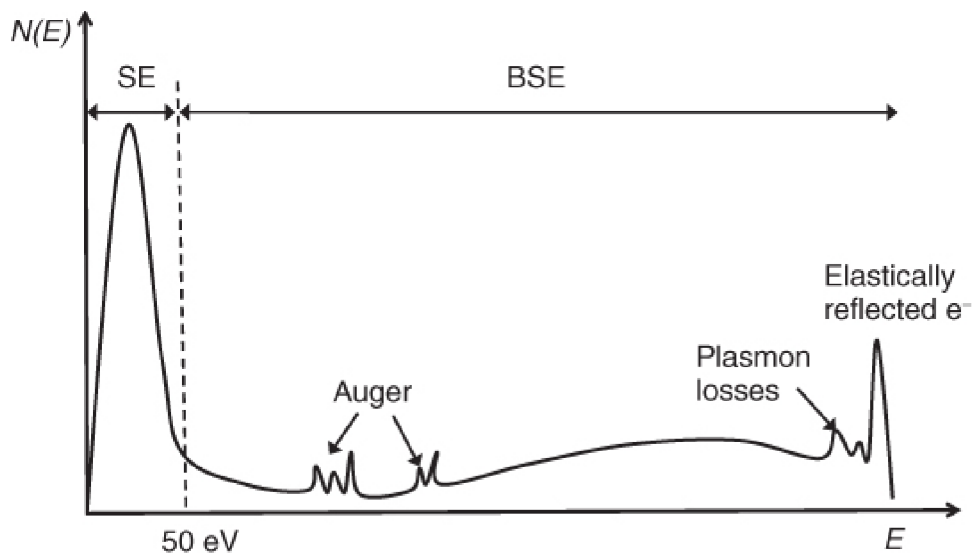

Figure 3.3: Histogram of energy of signal electrons (SE, BSE and Auger electrons) [34].

3.2 Secondary electrons

Secondary electrons are produced when weakly bound valence electrons or conduction band electrons are ejected by inelastic scattering. The quantity of secondary electrons emitted by the specimen N_{SE} divided by the total number of primary electrons N_{Prim}, which make up the incident beam, is known as secondary electron yield δ

$$\delta = N_{\text{SE}}/N_{\text{Prim}}, \tag{3.2}$$

as it was proposed in [32]. The transfer of kinetic energy from the primary electron to the SE is relatively small because of the significant mismatch in relative velocities between the primary beam electron and the weakly bound atomic electrons. As a result, the SEs are ejected with low kinetic energy. They must move through the specimen after being ejected while undergoing inelastic scattering, which reduces their kinetic energy even more. Because of this, only SEs that are formed close to a surface have a good possibility of escaping, even if they are generated along the whole interaction volume. The initial kinetic energy, the depth of creation, and the characteristics of the sample material all affect the likelihood of escape. In [35],there is a model proposed, that shows the dependency of escape depth d_{Esc} in nm on A (the atomic weight in g/mol), ρ (the density in g/cm^3), Z (atomic number), and I (first ionization potential in eV):

$$d_{\text{Esc}} = \frac{0.276AI}{\rho Z^{0.66}}. \tag{3.3}$$

The tilt of the sample affects the yield, and a straightforward geometric reasoning can explain this dependence. In Figure 3.4, it is visible that the path in the area of SE escape depth of primary electrons that immerse under the surface under perpendicular incidence is shorter then in the case of an incidence at an angle α. The path s then depends on the tilt angle according to the equation

$$s = d_{\text{Esc}}/\cos\alpha. \tag{3.4}$$

Geometry is similar if we discuss the path along which electrons come out of the sample. It is anticipated that the angular distribution of released secondary electrons will follow a cosine distribution with the emergence angle in regard to the local surface normal because the chance of secondary electron escape reduces as the escape path length increases. Cosine distribution is depicted in Figure 3.5. With lower beam energy, the range of the beam electrons is reduced, more of that energy is deposited and more secondary electrons are generated in the near surface region, from which secondary electrons can escape. Together with the fact that the rate of energy loss increases, it shows that SE yield increases with decreasing primary energy. Secondary electrons can be generated by BSE in addition to primary electrons. This type is called SE$_2$ and has the same distribution as BSE and thus carries the same information.
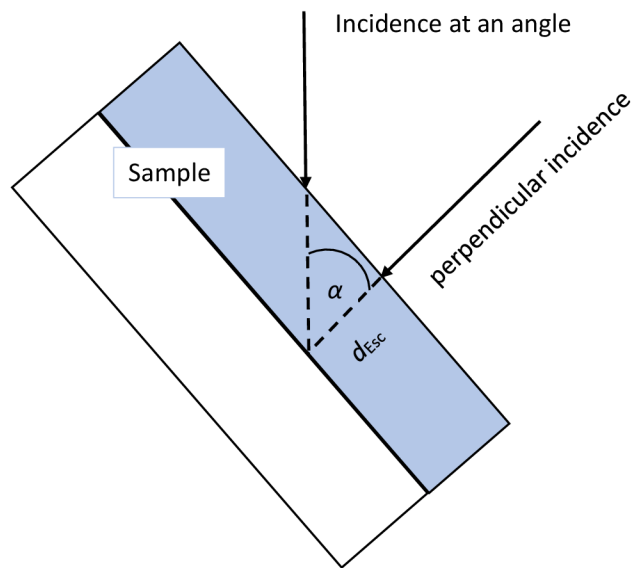
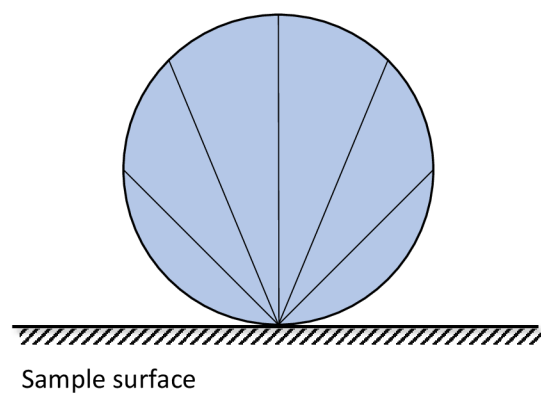Figure 3.4: Scheme of sample tilt and its implications on SE yield.

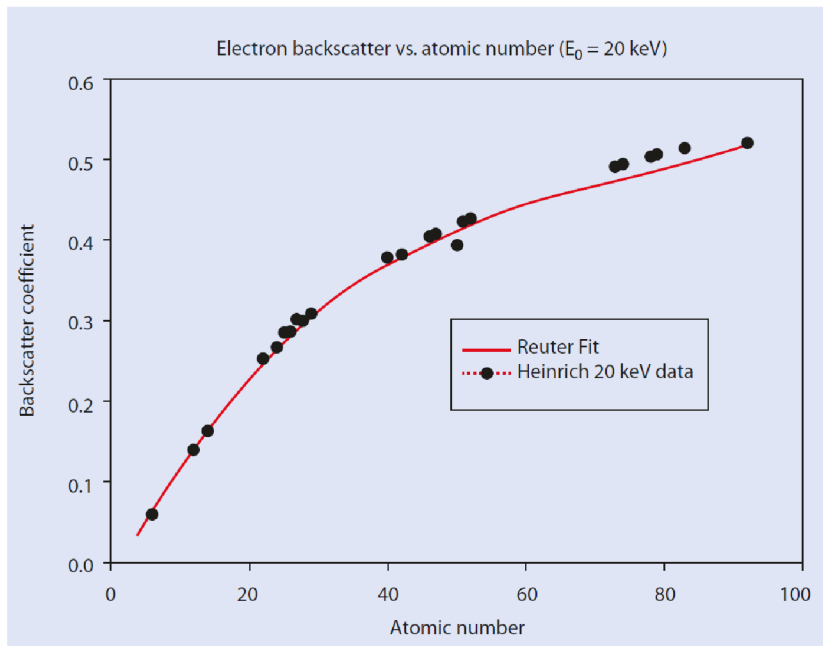Figure 3.5: Cosine distribution. The straight lines describe probability of emission of a secondary electron.

Figure 3.6: Backscattered electron coefficient η dependency on atomic number Z [32] measured by Heinrich [36] and fitted by Reuter [37].

3.3 Backscattered electrons

A sizeable portion of the incident beam electrons experience enough scattering events for them to entirely change their direction of passage in the specimen, returning to the surface and leaving the specimen. These electrons are called backscattered electrons (BSE). The backscattered electron coefficient η, which is defined as the fraction of number of BSE electrons N_{BSE} and the total number of primary electrons N_{Prim}, is defined as

$$\eta = N_{\mathrm{BSE}}/N_{\mathrm{Prim}}. \tag{3.5}$$

This essentially refers to the likelihood that an electron will backscatter and leave the surface, which can be described by integration over probability of finding an electron in a certain range of energies or a solid angle. Due to the complexity of this probability function, it is often necessary to split the spatial and energy distribution problems and address them separately. Heinrich used a beam energy of 20 keV to do in-depth experimental observations of the backscattered electron coefficient as a function of the atomic number Z on flat pure element targets [36]. Seven years later, there was a fit for the data provided by Reuter [37], which resulted in equation

$$\eta = -0.0254 + 0.016 * Z - 1.86 * 10^{-4} * Z^2 + 8.3 * 10^{-7} * Z^3. \tag{3.6}$$

The data and the fit are displayed on Figure 3.6. Fit allows us to determine the coefficient of an element that has not been directly measured and to estimate the intensity change at junction between any elements. This reliance does not significantly alter for different primary beam energies. Combinations of various elements and compounds have been demonstrated to have a coefficient η_{mix} that is equal to the sum of the coefficients of the individual elements η_i weighted by their concentration C_i

$$\eta_{\mathrm{mix}} = \sum \eta_i C_i. \tag{3.7}$$

The backscattering coefficient of thin films of thickness t is given by formula

$$\eta(t) = \frac{\lambda^4}{16\pi^3 a_H^2} N Z^2 t, \tag{3.8}$$

where N is the number of electrons per unit volume, λ denotes the de Broglie wavelength and a_H is the Bohr radius of the hydrogen atom [9]. In the case that we observe objects proportionally smaller than the background, we describe the contrast K with Weber's formula

$$K = \frac{I - I_b}{I_b}, \tag{3.9}$$

where I_b is the background intensity and I is the intensity of the observed feature [38]. The formula would look the same for the case that we are not talking about the background and the object, but about two objects, with one having a greater intensity than the other. So in case of $I_2 > I_1$, we get

$$K = \frac{I_1 - I_2}{I_2} = \frac{\eta_1 - \eta_2}{\eta_2}. \tag{3.10}$$

and it is analogous that the contrast between materials with coefficients $\eta_2 > \eta_1$ will correspond to the equation as well. Here we are talking purely about material contrast or Z contrast. In practice, this means that we measure flat polished samples without the influence of topographic contrast, and then the relation in Equation 3.10 describing the contrast applies.

The topographic contrast can be described by examining the angular distribution of BSEs and the dependence of η on the tilt angle ϕ of the flat surface of the sample. It was shown that in the case of a normal incidence, where the beam falls perpendicular to the plane of the surface, the angular distribution obeys Lambert's cosine law proposed in [39] as

$$\frac{\mathrm{d}\eta}{\mathrm{d}\Omega} = \frac{\eta}{\pi} \cos\phi. \tag{3.11}$$

The cosine distribution has been shown to have the shape of a sphere above the sample before in section 3.2, Figure 3.5. At a different angle of incidence, the distribution has two components. One is formed by the cosine distribution caused by diffusion scattering in the material. The second part extends the distribution in the direction of reflection. This distribution is created by electrons from a smaller depth that have gone through fewer scattering events. In Figure 3.7, there is depiction of angular distribution for three different angles of incidence. We see that the second component of the dependence, which corresponds to the reflection, increases with the angle of incidence. On the polar diagrams, we also see different elements and the fact that heavier elements tend to lean towards a cosine distribution. The dependence of the total η on the proton number Z can be seen in the case of perpendicular incidence in the form of a circle size above the sample. What is interesting at higher angles of incidence is that even though the overall η is higher for a heavier element, a lighter element can have a greater yield in the direction of reflection, as we see for example with beryllium and gold at an angle of incidence of 80 degrees. If we had a detector that collects the signal only from a selected interval of angles, we could achieve that the light element in the image would be brighter than the heavy element. It shows the importance of detector features such as size and position in creating contrast. An analytical description of this distribution does not yet exist.
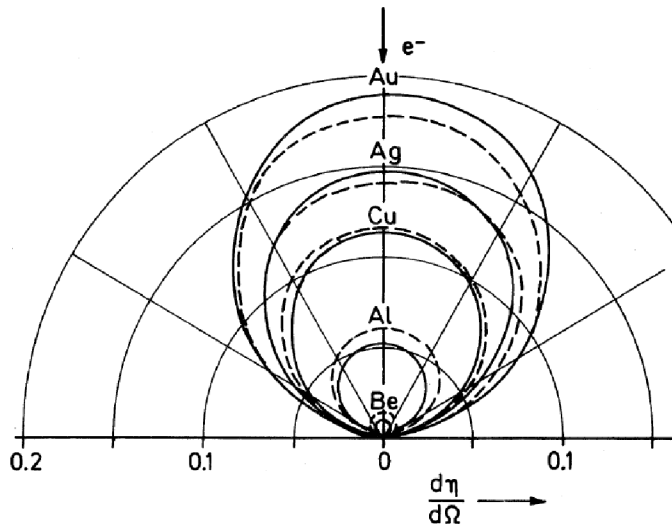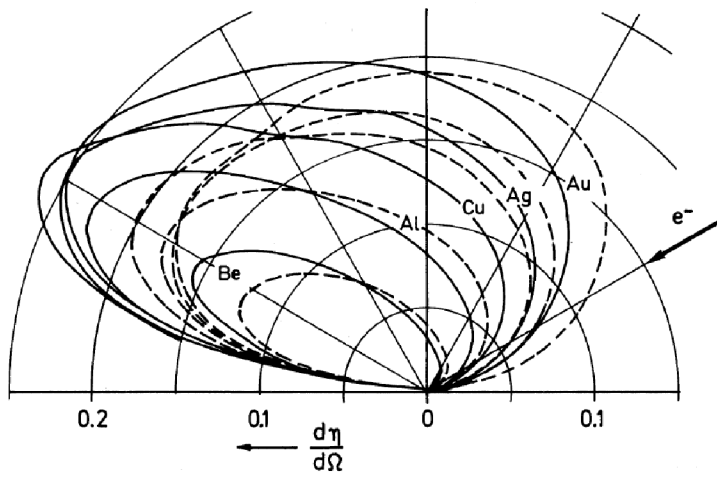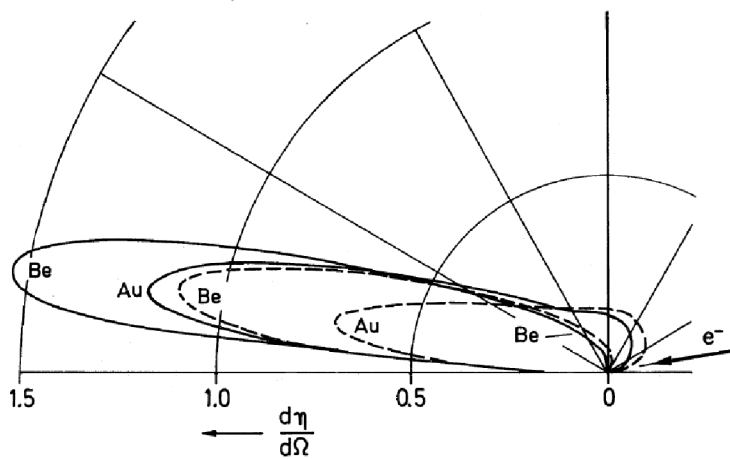
Figure 3.7: Polar diagrams of angular BSE distribution $\frac{d\eta}{d\Omega}$ for different tilt angles: (a) 0°, (b) 60°and (c) 80° [9].

24

There are several possible relations describing the dependence of the total η on the angle of incidence ϕ. There is a formula derived by an experiment in form of

$$\eta(Z,\phi) = (1 + \cos\phi)^{-9/\sqrt{Z}}. \tag{3.12}$$

proposed in [40]. Another was originally derived for SE in the form

$$\eta(Z,\phi) = \eta_0(Z)\mathrm{e}^{\gamma l(1-\cos\phi)}, \tag{3.13}$$

where η_0 is η for perpendicular incidence, γ refers to an absorption coefficient and l is a diffusion range [41]. These equations fit the data for primary energies greater than 5 keV. In Figure 3.8, we see the dependencies depicted separately.

Another parameter worth investigating is the depth distribution of backscattering. Bethe's law describes how a charged particle loses energy per unit distance when passing through matter and Rutherford cross section is the basis for describing angular scattering [42]. Electrons undergo multiple scattering events. Elastic scattering only deflects electrons by a small angle, while inelastic scattering can deflect them by a larger angle. Electron paths at a certain depth become isotropic and they further move isotropically in all directions until their energy approaches zero. The Bethe range S_B is the total range of electrons along their complete route up to their thermalization point, and the depth range R is the distance from the surface to this point [43]. S_B can be described by

$$S_B = \int_{E_0}^{0} \overline{\frac{\mathrm{d}s}{\mathrm{d}E}}\mathrm{d}E, \tag{3.14}$$

where $\overline{\frac{\mathrm{d}s}{\mathrm{d}E}}$ refers to averaged energy loss $\mathrm{d}E$ per unit path $\mathrm{d}s$ and can be expressed by Bethe law as

$$-\frac{\mathrm{d}s}{\mathrm{d}E} = 7.85 * 10^4 \frac{\rho Z}{AE}\ln(1.165E/J), \tag{3.15}$$

where ρ is density of the target in g/cm^3 and J refers to ionization potential approximately corresponding to $0.0115Z$ keV. From Equation 3.14 and Equation 3.15, we can obtain S_B numerically because the integral cannot be expressed in terms of elementary functions. Alternatively, we could use simplified relation

$$S_B[\mathrm{nm}] = \frac{85AJ^2}{\rho Z}\left(\frac{E_0}{J}\right)^{1.7}. \tag{3.16}$$

In experiments, it is impossible to directly measure the entire S_B range. Therefore, the only way to compare the calculated values of S_B is with the outcomes of Monte Carlo simulations.

The energy spectrum of emitted electrons was shown in Figure 3.3. However, the dependence on material and primary energy was not discussed there. In Figure 3.9, we can see that the main peak is moving towards the primary energy with Z number of the sample until finally it merges with the elastic peak as we see in the case of gold. The elastic peak with the electron energy equal to that of primary electrons is getting more visible with Z. How distinctly we see the elastic peak is also affected by the primary energy of the beam and the angle of incidence. The elastic peak can be best resolved for energies $E < 5$ keV [9].
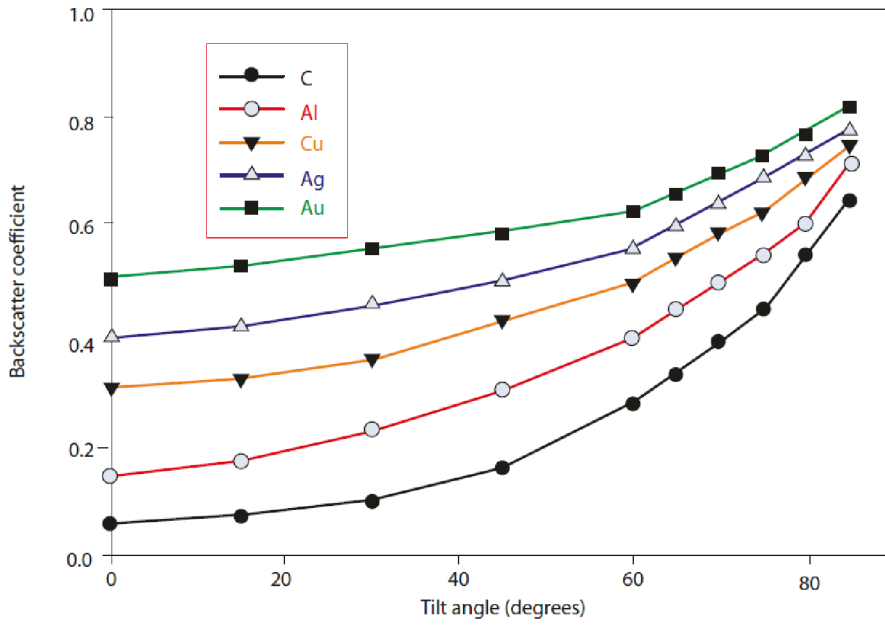
(a)

(b)
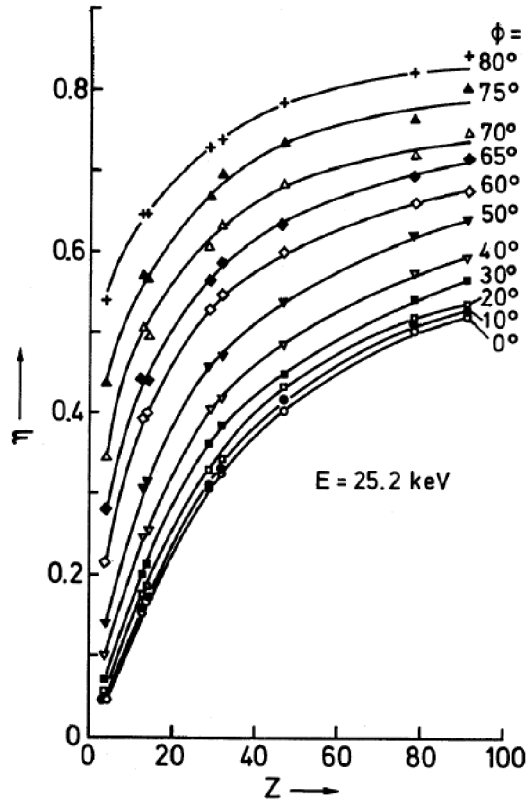
Figure 3.8: Backscattering coefficient η dependence on (a) proton number Z for different angles of incidence ϕ [9], (b) on angle of incidence ϕ for different elements [32].
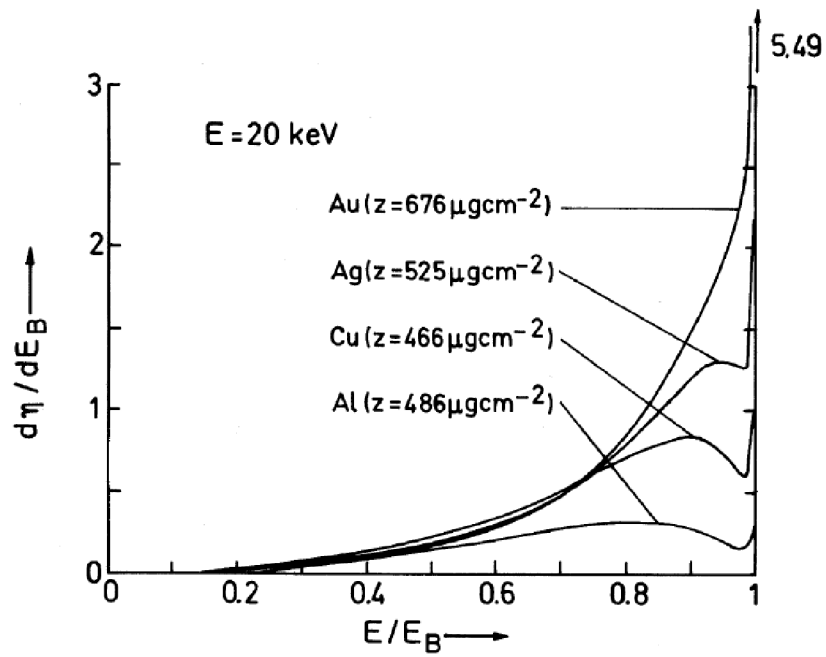
Figure 3.9: Backscattered electron energy distribution for different materials [9].

The specimen's composition, topography, and crystallography can all be inferred from the BSE signal. Usually, topographic contrast is discussed in relation to secondary electrons, however the amount of detected backscattered electrons and their spatial distribution are also influenced by the tilt of the sample surface. However, they show a stronger response at the junction of materials with different atomic numbers. In the case of displaying a sample with varied topography and composition, it is very difficult to distinguish which type of contrast is involved in specific areas of the sample. Samples having the same composition and varying topography or polished samples with varying composition are less challenging to describe. Therefore, at the beginning of the task of performing measurements and comparing them with simulations, it is better to use such samples to eliminate the complexity of the resulting image.

Chapter 4

Simulations of BSEs

4.1 Methods

The methods of simulating the interaction of electrons with the sample can be divided into analytical and numerical. Analytical models of complex system behavior can be expressed as logical conditions or functional relations. When there is a clear relationship between the parameters of a complex system and the study's initial circumstances and the unknown values, the investigation can be carried out to the fullest extent possible. It is quite challenging to build an analytical model for complicated systems. When building an analytical model, it is necessary to make crucial simplifications that could unfortunately prevent the model from accurately describing the process or phenomenon. It is necessary to use numerical simulation when the phenomena in a complex system are so complicated that the analytical model can no longer accurately represent reality [44].

In the numerical simulation model, a set of algorithms represent the behavior of a complex system's parts and then simulate the events that might occur in the real system. The values of system parameters represent genuine phenomena in the system and provide knowledge about possible behavior of a complex system in this specific situation. Modeling methods allow you to input data containing information about the beginning state of a complex system.

A large group of computational techniques known as Monte Carlo methods rely on repeated random sampling to produce numerical results. The core idea is to leverage randomness to find solutions to issues that, in theory, may be deterministic. They are frequently applied to mathematical and physical issues. Taking samples from a probability distribution, numerical integration, and optimization are the three problem types where Monte Carlo methods are most frequently applied [45]. Monte Carlo methods are effective for simulating systems with many degrees of freedom in physics-related problems.

Although Monte Carlo techniques differ, they frequently have the following characteristics. Firstly, a range of potential inputs must be established, then inputs are randomly generated from a probability distribution over the domain. A deterministic computation is performed on the inputs and the outcomes are aggregated. The quality depends on the random number generator used and the amount of data generated. It is always true that the more data we provide, the more precise the outcome will be.
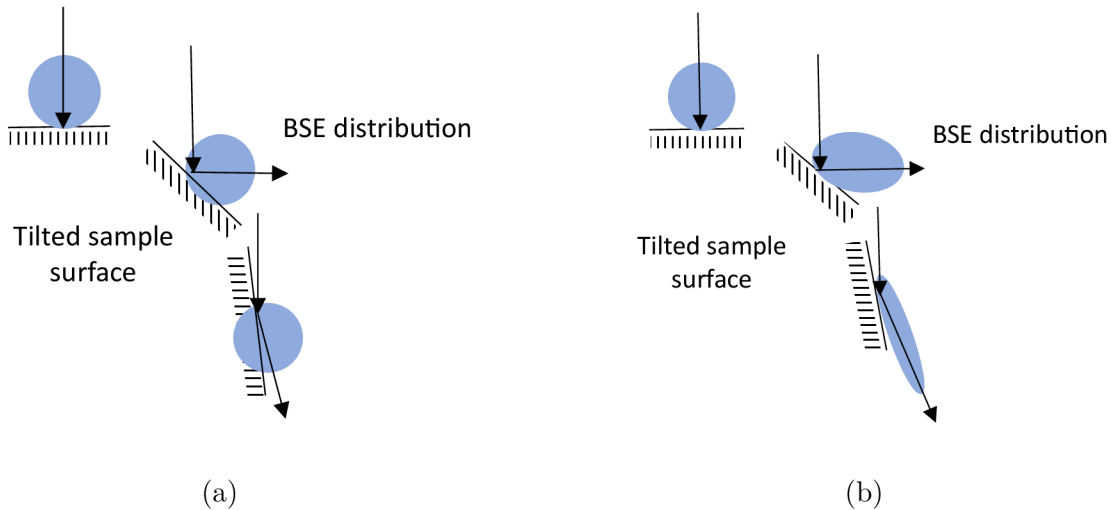
Figure 4.1: Scheme of two models of BSE distribution: a) tilted cosine distribution, b) tilted cosine distribution with impact rebound mechanism.

Random number generators can be divided into two categories: pseudo-random generators and true random number generators. Pseudo-random generate numbers based on an algorithm while true generators use a truly random often physical principle. In general, pseudorandom is sufficient for Monte Carlo purposes, however, it is necessary to make sure that it generates points with the correct probability distribution.

4.2 Simplified model of backscattered electron emissivity

As described in section 3.3, there is no accurate analytical model for BSE electrons that would describe their spatial distribution. To start building an analytical model, a cosine distribution (Equation 3.11,Figure 3.5) with a volume proportional to the backscattering coefficient (Equation 3.5) is worth considering. This model is valid in the case of a perpendicular impact, but for simplification there is an option to apply it also for an impact at an angle in the form of tilting the given cosine distribution.

For further improvement of this model, it could be composed of two parts. One would correspond to a cosine distribution and the other would stretch the distribution in the direction of reflection given by the angle of incidence. The coefficient could change with the angle so that the reflection mechanism would prevail as the angle increases. With this approach, the question arises as to how to change this coefficient in order to obtain a result similar to reality. In Figure 4.1, we can see how the two different approaches play out on a surface that is not tilted, slightly tilted and very tilted. In a) subplot, we are only using tilted cosine distribution and in b) subplot there is an effect of reflection added.

This simplified model can then be used to simulate images. It involves generating random electrons corresponding to this analytically described distribution. The advantage of the analytical approach is its universality. Therefore, it is less computationally

demanding to apply a simplified model to this chain rather than running a numerical simulation for each specific case. However, it is clear that accuracy is sacrificed and it is always necessary to take into account important variables such as the primary energy of the beam.

I created a simulation of a ball using a simple model with a tilted cosine distribution. I did not take energy distribution into account, but took data with random electron directions corresponding to a cosine distribution. With a step of five degrees, I tilted the data and took the angular acceptance of T1 detector into account as if the ball sample were 10 mm far from the pole piece. The intensity points in the intensity profile in Figure 4.2 subplot a) are then total number of detected electrons normalized so the peak intensity is 1. I provided a polynomial fit for the data and based on that created a simulated image of a ball which is in the b) subplot. I got the image from the intensity profile using three nested for cycles. First, I prepared a field of zeros 1000x1000, the first cycle went from 0 to 400 and represented the radius r of the investigated area, then two cycles went through the x and y positions in the prepared field and when $\sqrt{x^2 + y^2} = r$, the corresponding fit value $intensity fit$ was assigned to the field. The fitting function was also defined in 400 points so it corresponds to the number of steps in r. The loop is shown below in Listing 4.1.

Listing 4.1: A loop used to create an image of a tin ball from intensity profile described by fit function.

```
image = numpy.zeros([1000, 1000], dtype = float)
for r in range (0,400):
 for x in range (0,900):
  for y in range (0,900):
   if int(math.hypot(x-500, y-500)) == r: image[x,y]=intensityfit[r]
```

## 4.3 Model of backscattered electron emissivity based on Monte Carlo results

4.3.1 Software packages

There are several software packages available for electron beam-matter interaction simulation such as Casino and Nebula. I mainly used Casino software to simulate the interaction of primary electrons and the sample. Versions 2.51 and 3.3 are currently available [46] and it has been shown that only version 3.3 is suitable for 3D analysis [47]. Although version 2.51 generates 3D data, the BSE spatial distribution repeatedly came out asymmetrical, which is not the case when using version 3.3. However, it can be used effectively for 2D visualization of the interaction volume.

Two computational factors are involved in simulating the electron trajectory in a three-dimensional material. The first one is the computation of the ray tracing inside the sample and the second factor is the actual physical interaction with the material inside the sample. For manual processing, all the data from the stored electron trajectories, including each scattering event's position and energy, can be exported as a text file. Combining fundamental 3D forms and planes allows for the creation of the 3D sample modeling. Each shape has a position, a dimension, and an orientation that define it. Casino utilizes OpenGL technology to display the sample [48]. In Figure 4.3, there is
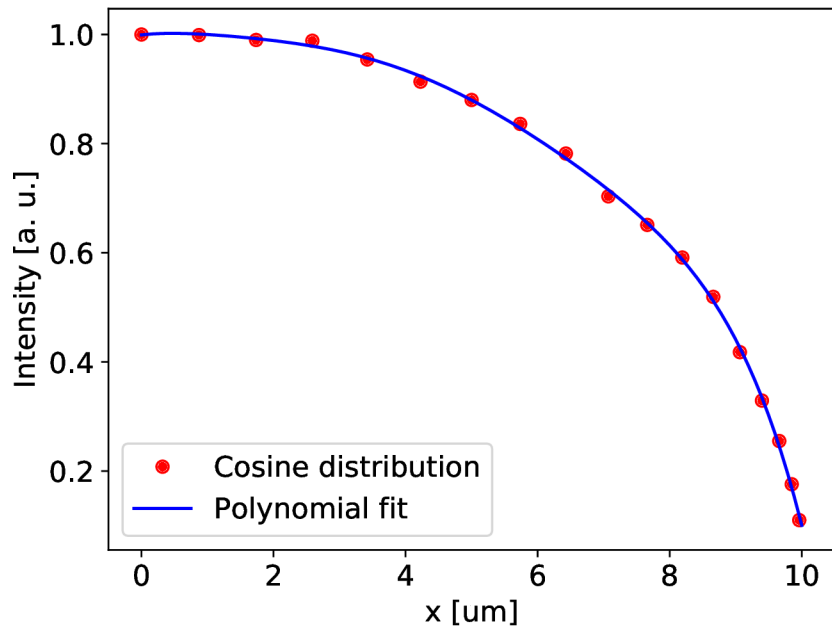
(a)
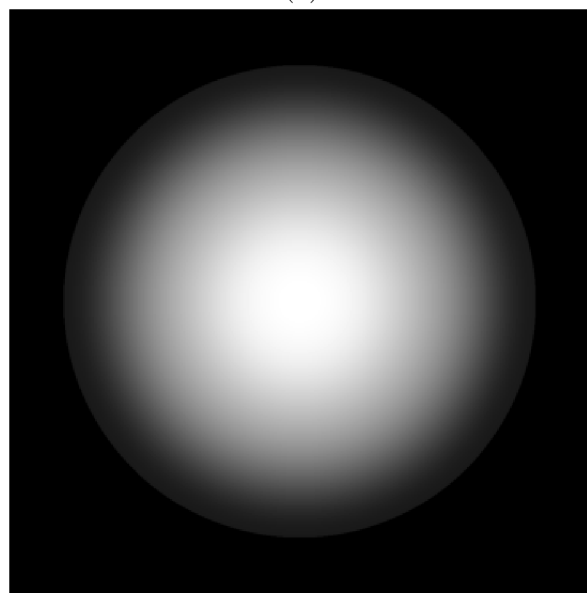
(b)

Figure 4.2: Ball with a 10 μm radius a) intensity profile with polynomial fit and b) image simulation. Simulated as if it was detected by T1 detector and the ball sample was 10 mm far from the pole piece.

an illustration of what the user interface of the program looks like and how the sample is displayed. We see a box there, which I defined as aluminum and has a size of 5 μm. Landing energy of the beam is 10 keV. The input beam comes from the negative side of the z-axis and passes through the origin of the coordinate system. This geometry cannot be changed, only the semi-angle and the diameter of the beam can be adjusted, but it cannot be tilted or shifted in any way. Tilt and shift must be defined on the sample. The input beam is marked in black, the absorbed electrons in blue and the BSE in red. There are more marking modes, for example collisions can be displayed. In Figure 4.4, there is a depiction of interaction volume in the case of Al flat sample with primary energy 10 keV at perpendicular impact. There are 10 000 trajectories simulated in Casino v2.51, the blue ones represent absorbed electrons and the red ones backscattered.

There are seven basic shapes available: plane, box, pyramid, sphere, cylinder, cone, and rounded box shapes. After the creation of the sample is finished, all the shape surfaces are transformed into triangles, because this simplification is necessary for ray tracing algorithm usage [49]. For each generated electron, the intersected triangle is determined by testing each triangle using a vector product. To make this process faster, the triangles are organized in a 3D partition tree, where each partition contains ten triangles [47]. The composition can be set as a single element or multiple elements like a molecule or an alloy. The mass density of the region can be defined by the user or obtained from a database and in case of multiple elements either the atomic fraction or the weight fraction can be used to set the concentration. Scanning and image simulation is also possible as well as secondary electron generation, but it takes a lot of computational power.

Trajectory of the electron in the specimen is defined by scattering events. Inelastic scattering is approximated by mean energy loss between two elastic events. The angle and the distance between two events are determined by random number with defined probability distribution. The events are happening as long as the electron does not leave the sample or is not trapped inside the sample, which happens when the energy is below a threshold value of 50 eV. Scattering cross-sections are handled via databases of values calculated by ELSEPA software [50]. The hybrid energy loss model was added for SE generation. The fast SEs are calculated according to the Möller equation and the slow SEs are generated using the plasmon theory [51]. MONSEL code from NIST is utilized for implementation [52].

Casino offers the option of displaying several types of charts. There is also the possibility to download the data in the form of a text document. An illustration of the text document and the information it contains is shown in Figure 4.5. Information is divided by scan point and inside it by trajectory number. For each trajectory, we have information about every collision. We have the position in space given by the coordinates X, Y, Z, then the direction cosines the electron has after the collision Rx, Ry and Rz. Another important data is the energy after the collision and the type of collision. There are also four possible categories trajectories are divided into. They are addressed as "Type" below the trajectory number. "Simple" is the label for absorbed electrons, the energy of which dropped to 50 eV, then there is "Backscattered" and "Transmitted" category and in case of SE generation "Secondary electron" label.
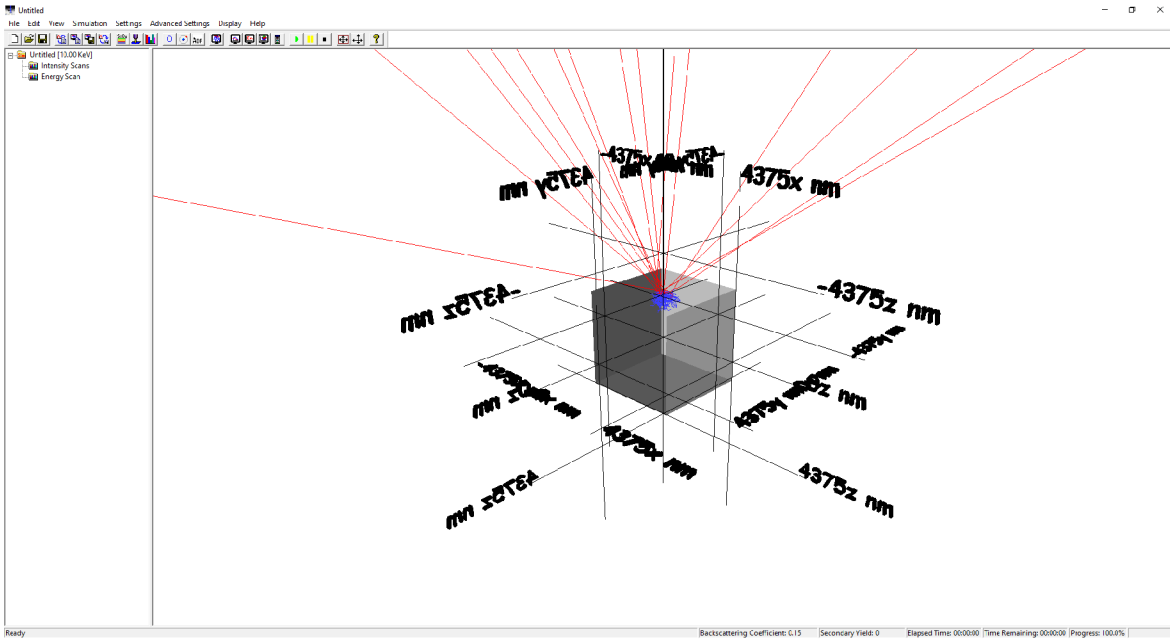
Figure 4.3: Illustration of Casino v3.3 UI environment. Beam with landing energy of 10 keV (black line) penetrates aluminium box with size of 5 μm (grey). Absorbed electrons are depicted blue and backscattered electrons red.
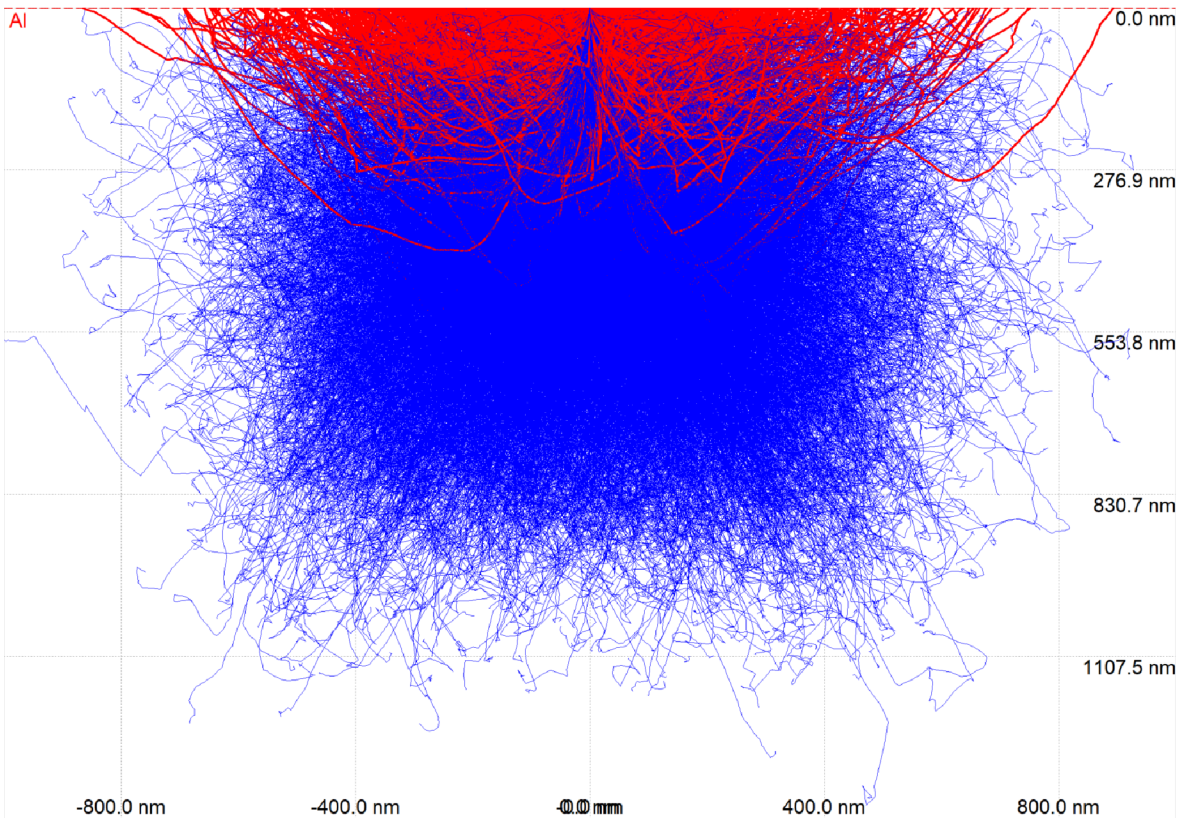

Figure 4.4: Simulated interaction volume for Al with primary energy 10 keV at perpendicular impact. Red lines depict trajectories of BSE in the sample, blue are absorbed electrons.

The energy and spatial distributions of BSE generated by Casino software were compared with Nebula software. Nebula is an open-source software package with first-principle physical models that may be used with multi-core CPUs or GPUs [53]. The essence of Nebula's approach to simulating interactions is similar to that of Casino. Discrete events of electron scattering occur across the material's volume. Between these instances, the electron is handled as though it were in free flight. Every electron is treated independently. However, software and user input are handled differently. The user provides three files to Nebula. The first one describes the geometry of the sample and the detector and then there is a file with primary electrons describing their energy and geometry. The last file is generated by cstool, which based on material parameters compiles scattering cross sections. Nebula then processes this input and generates a list of detected electrons and their properties such as energy, position and direction. Nebula software was used only to compare the resulting BSE electron distribution with Casino generated one.

4.3.2 Data processing and visualization

I wrote a script to parse data in the output Casino text file by dividing the text by trajectories and then by tabulator, taking the last direction and energy for each trajectory. The coordinates are defined in the Casino so that the direction of the beam is the direction of the z axis. Rz is therefore always negative for BSE. This direction is not related to the normal of the sample but always to the beam. It creates a bit of a problem in that if the sample is tilted, BSEs that point in the direction of the positive z-axis are also created, but Casino does not consider them as BSEs and therefore they are not marked accordingly either on the chart or labeled in the text file. Instead of "Backscattered" they are labeled as "Simple". I used additional filtering according to the angle and energy to separate these electrons from the ones that were absorbed. The condition was that the energy was larger then 0.05 keV. In this step, I wanted to get all BSEs and not yet apply filtering based on detector acceptance. This is how I obtained separate files with information about the direction and energy of the BSE. Next, I transformed the data into spherical coordinates as needed. Basic overview of the script is placed below in Listing 4.2.

Listing 4.2: Part of a script used for data acquisition from a text file generated in Casino.

```
f = open(pathtotxt)
data = f.read().split("Trajectory")
data = numpy.array(data)
data = numpy.char.replace(data, '\n', '\t')
file = open(path2 + "Energy,Rx,Ry,Rz.txt", "a")
for i in range(1, len(data)-1):
 dat = data[i].split("\t")

 if dat[5] =='Backscattered':
  file.write(dat[-5]+'\t'+dat[-8]+'\t'+dat[-7]+'\t'+dat[-6]+'\t'+'\n')

 elif (float(dat[-5])>0.05) :
  file.write(dat[-5]+'\t'+dat[-8]+'\t'+dat[-7]+'\t'+dat[-6]+'\t'+'\n')
```

Then the goal was to visualize the spatial distribution of BSE emissivity. I created a 3D histogram where the individual bins are given by sections of azimuthal angles. The angles were chosen in a way that the surface of each bin is the same. I divided the

```
"Scan Point"      0      " Trajectories : "
"##############################################################
#"
"-----------------------------------------------------------
"
"Trajectory"      0

"Type : "
        Backscattered

"Collisions"

"X"   "Y"   "Z"   "Rx"   "Ry"  "Rz"  "Energy"     "CollisionType"
-0.228235   0.134503   0      6.32598e-010       4.99635e-009      1
      10    Region
-0.228235   0.134503   4.94314     0.00561252 0.00263526 0.999981
      9.96228293984    Atom
-0.222171   0.13735    6.0235      -0.022217   -0.0336466 0.999187
      9.95401768454    Atom
-0.243724   0.104709   6.99282     -0.0420391 -0.002879050.999112
      9.94659174569    Atom
-0.24788    0.104425   7.0916      -0.067433   0.084535    0.994136
      9.94583459926    Atom
```

Figure 4.5: Casino output text document sample.

steps in θ which corresponds to $\arcsin(dz)$ equally from 0 to 90°. If N_θ is number of steps in θ, number of steps in ϕ for given theta to keep surfaces equal would be

$$N_\phi = 4N_\theta \cos(\theta). \qquad (4.1)$$

At the moment I utilized spherical coordinates and used *theta* and *fi* calculated from Rx, Ry and Rz. In two immersed for cycles, I found out which bins individual electrons fall into and accordingly added the number of electrons to the field r which represented the radius or distance of the bin from the origin point. I also calculated the average energy of the electrons in the bin. For the 3D graphic display, I went back to Cartesian coordinates. A sample of the part of the code from the transition to spherical coordinates to return to Cartesian coordinates is located in Listing 4.3 . The input were arrays Rx, Ry, Rz, and *energy*. After this code sample, the fields were displayed in a scatter plot, with the color parameter being described by the *endist* field which represents the average energy in the bin.

Listing 4.3: Skript used for 3D histogram display.

```python
fi = numpy.arctan2(Ry, -Rx)+numpy.pi
theta = numpy.arcsin(Rz)
steps = 10 #number of steps in theta
dtheta = numpy.pi/2/steps

#number of the interval theta belongs to
thetaindex = numpy.array(theta/dtheta, dtype=int)
#creation of theta array in the histogram
thetas = numpy.linspace(dtheta/2, numpy.pi/2-dtheta/2, steps)
#number of fi steps for given theta
finof = numpy.array(numpy.cos(thetas)*(steps*4), dtype=int)
r = numpy.zeros((steps, steps*4)) #radius array
endist = numpy.zeros((steps, steps*4)) #average energy array

#cycle that assigns electron to bin
for i in range(0,steps):
```

36

```python
    indexes = numpy.where(thetaindex==i)[0]
    en=energy[indexes]
    data = fi[indexes]
    dfi = numpy.pi*2/finof[i]
    fiindex = numpy.array(data/dfi, dtype=int)
    for j in range (0,finof[i]):
      indexess = numpy.where(fiindex==j)[0]
      endist[i][j] = numpy.sum(en[indexess])/len(indexess)
      r[i][j] = len(indexess)

r = r/numberoftrajectories #normalization of size
#transformation back to Cartesian coordinates
x = numpy.zeros((steps, steps*4))
y = numpy.zeros((steps, steps*4))
z = numpy.zeros((steps, steps*4))
for l in range(0, steps):
  for m in range (0, finof[l]):
    x[l][m] = math.cos(m*2*math.pi/finof[l]) * math.cos(thetas[l]) *r[l][m]
    y[l][m] = math.sin(m*2*math.pi/finof[l]) * math.cos(thetas[l]) *r[l][m]
    z[l][m] = math.sin(thetas[l]) *r[l][m]
```

Examples of the histogram are displayed in Figure 4.6 for angles of incidence 0°, 60° and 80°. Angle of incidence is the angle between the incident beam and the surface normal. It is shown for single-element flat samples composed of Au and Al. The color indicates the average energy of electrons emitted out in the section of these directions. The beam impacts the sample at the origin of the coordinate system and the distance of the colored points from the origin of the coordinates represents the number of electrons in a given bin divided by the total number of BSE electrons. So the values on the x, y, and z axes are basically marginal probabilities. The surface of the sample in this coordinate system is represented by the xy plane. Perpendicular impact is a good test for both the correctness of the Monte Carlo-generated distribution and the correctness of the histogram displaying. It should have an appearance of a cosine distribution. Due to randomness, there will be inaccuracies in the shape of the histogram which should smooth out with larger number of data.

What we can determine from the histograms are basic principles of dependencies of the BSE distribution on element and its atomic number and on the angle of incidence. As expected, with higher angles the distribution is no longer close to cosine distribution and is stretched in the direction of reflection. This is for both elements visible at the angle of incidence 80°, but with gold the tendency is to linger more to the cosine distribution with rising angles. The energy is highest in the direction that is closest to the original direction of the beam.

In Figure 4.7, we can see energy spectrum for perpendicular incidence on a flat sample of Sn. There is a comparison of result obtained from Casino and from Nebula software. I believe, that this is the point where lies the biggest difference between the two softwares. Nebula always creates SEs as well as BSEs. I did not use the electrons that had lower energy that 50 eV, but electrons with slightly higher energy can still be generated based on the same principle. That is the reason why there is a peak in Nebula energy histogram and in Casino histogram, there is no such thing. Also histogram from Nebula includes an elastic peak which is never generated in Casino. With primary energy 10 keV, there should be an elastic peak, therefore it is conclusive that in this area Nebula has more effects included and generates spectrum closer to reality.
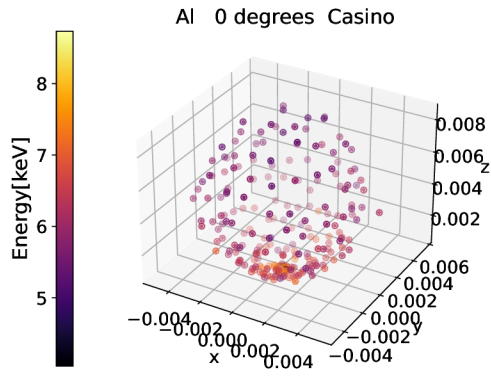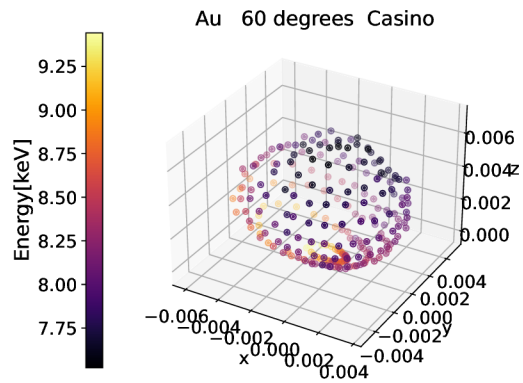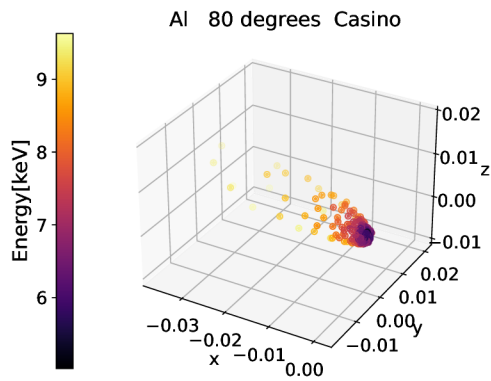
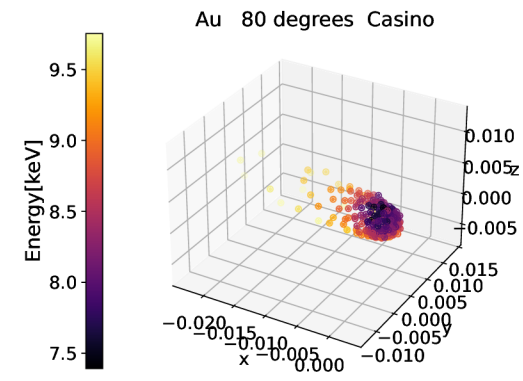(a) Al 0°
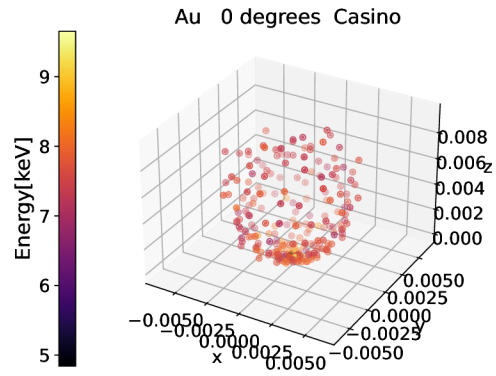
(b) Au 0°
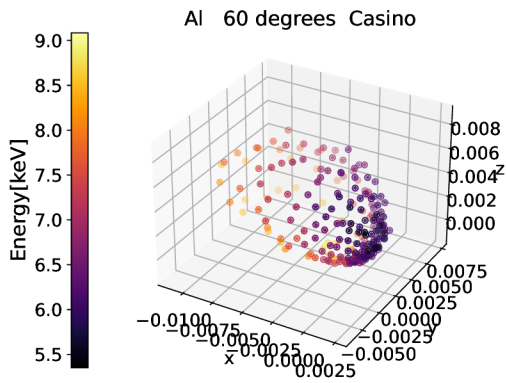
(c) Al 60°

(d) Au 60°

(e) Al 80°

(f) Au 80°

Figure 4.6: 3D histograms of BSE distribution for single element flat sample composed of Al and Au at angles of incidence 0°, 60°and 80°.

The typical peak that is visible in Casino histogram merged together with elastic peak in Nebula histogram, so that explains why the maximum is at different energy value. Nevertheless, the difference between Casino and Nebula shows only in two energy bins which overall does not create a major setback in Casino usage. Most of the simulations were made using Casino software.

4.4   Acceptance diagrams

Acceptance diagram is a two-dimensional description of detection possibilities of a certain microscope configuration. Different areas of the $E_k - \theta$ space are color coded. The E_k and θ coordinates denote kinetic energy and elevation angle of a signal electron, respectively. Acceptance diagrams differ for each detector and the accepted angles also change depending on the working distance. The input electrons must be defined and gradually traced under the given conditions, and based on whether their path ends at the detector, it is decided whether the electron of the given initial direction and energy is accepted. A sample of the acceptance diagrams for Apreo Standard and Optiplan usecase is shown in Figure 4.8. In Standard usecase, the booster tube is switched off and in Optiplan usecase the booster tube is brought to 8000 V. For the demonstration, I chose working distance 1 mm because the acceptance in angle is the most pronounced there. We also see that for the Standard usecase, the acceptance has the form of straight bands, so the accepted angles do not change depending on the energy. In the case of Optiplan, the energy dependence is visible. As mentioned, booster tube attracts high loss BSE, therefore the acceptance on T2 and T3 detectors is much more pronounced. Non-smooth transitions in the graph are caused by variable sampling.

This is only a graphic demonstration, but as a tool for further data processing I used a table that carries the same information. I took the list of BSE electrons, their energy as *energydata* array and theta angle as *thetadata* array, and iterated over them one by one in a for cycle. For each one, I found in the table the energy interval it belongs to in *energytable* array, and then I decided whether in this interval there are ones in $T1$ array. One means that the electron of given energy and angle would be detected. After that I decided whether the angle is in the accepted interval in the selected part (right energy interval and T1 equal to one) of *thetatable* array. In the case these conditions were met,variable *count* was increased by one. The part of the code in Listing 4.4 was also optionally included in a for cycle that goes over tilt angle of the sample. In the end of the script, there is a text file saved with number of counts for each tilt.

Listing 4.4: Part of a code that determines number of detected electrons.

```
for i in range (0, len(energydata)):
 diff = numpy.abs(energytable-energydata[i])
 indexes = numpy.where(diff==min(diff))[0]
 thetatable2 = thetatable[indexes]
 energytable2 = energytable[indexes]
 T12 = T1[indexes]
 indexes2 = numpy.where(T12==1)[0]
 if len(indexes) == 0: continue
 elif len(indexes2) == 0: continue
 elif thetadata[i] <= thetatable2[max(indexes2)]
  and thetadata[i] >= thetatable2[min(indexes2)]: count = count + 1
```

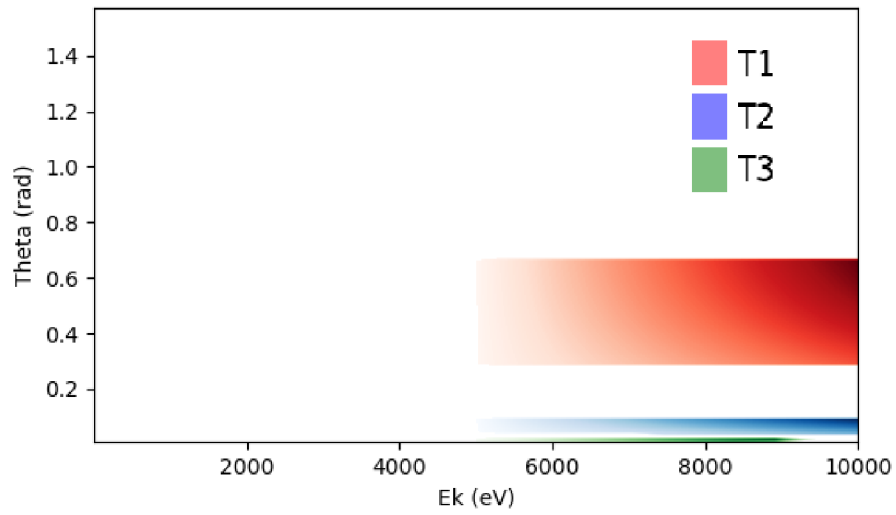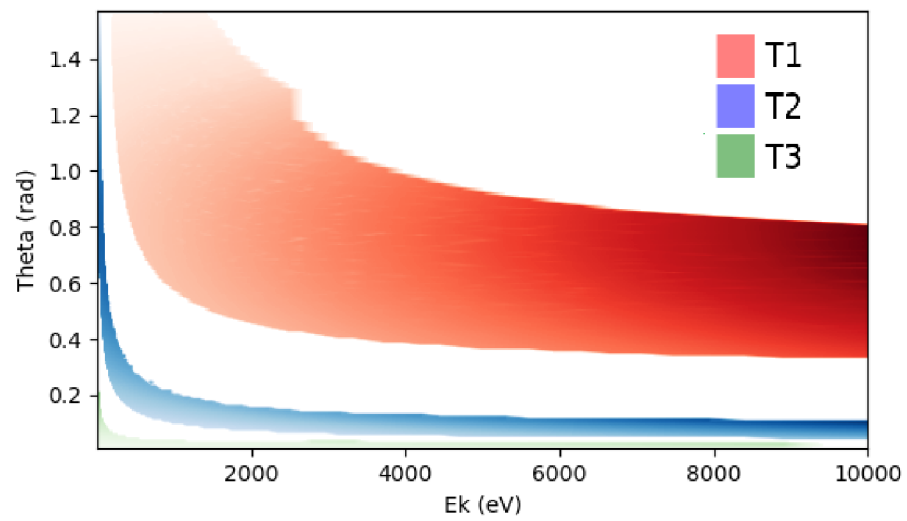I created more variants of the script. One that is geometrical without using acceptance
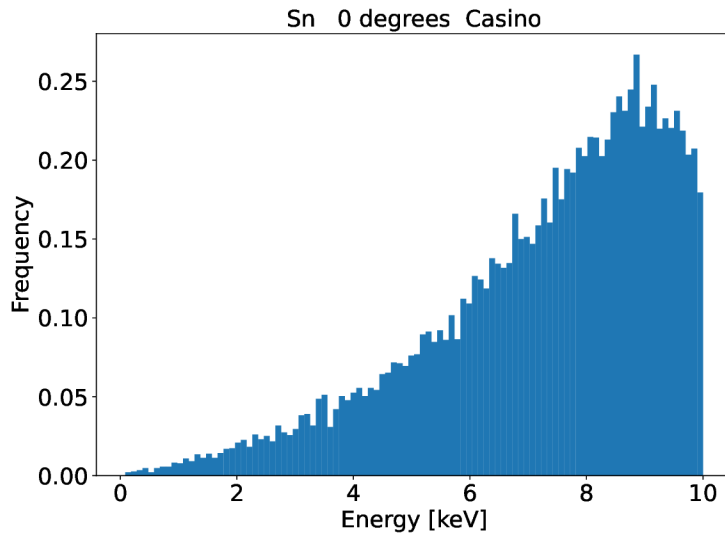
(a)
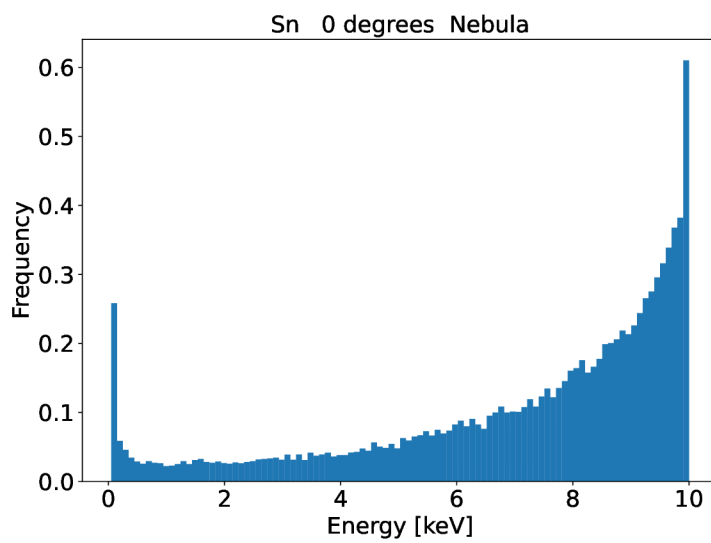
(b)

Figure 4.7: Comparison of energy histograms of perpendicular impact on a flat Sn surface from Casino and Nebula software packages.

Figure 4.8: Acceptance diagrams for Apreo WD 1 mm a) Standard usecase, b) Optiplan usecase.

diagrams at all for Standard usecase, one for Nebula, one for CBS detector and so on. The geometrical one was simply based on calculation of minimum angle of acceptance and maximum angle of acceptance based on geometry of the detector and working distance and then saving the number of trajectories that have the θ angle belonging to the interval. Again there was a for loop over tilt angles.

In order to simulate the intensity profile of a tin ball, I generated data for different inclinations of a flat tin surface with step 5°. I performed the procedure described above, so I received number of detected electrons for each tilt. It is necessary to make sure that we use the same number of primary electrons or the result needs to be normalized. In Figure 4.9, we can see simulations of intensity profiles of a tin ball based on data generated in Casino and processed trough acceptance diagrams for three different working distances WD 1 mm, 5 mm and 10 mm, so we can predict what the drop in intensity would be like when changing working distance. I converted the original dependence on the angle to spatial dependence on the radius of the ball. Even though the energy spectrum is different in the Nebula than in Casino, the intensity profile of the ball turns out the same.

The Figure 4.10 shows comparison of intensity profiles obtained using Casino simulations and a simple analytical model described in section 4.2. T1 acceptance diagram for 10 mm WD Standard usecase was used to proccess the data. It may seem strange that the tilted cosine distribution produces the same intensity profile as the distribution generated from Casino. As the tilt angle increases, we should get less intensity from the Casino distribution than from the cosine one, since the ellipsoid of the Casino distribution points away from the detector. However, in the case of the cosine distribution, I used the same number of BSE for all tilt angles, but in real life and in Casino we get more BSE electrons with the same number of primary ones with the tilt. This effect then balances out the influence of the shape of the distribution and in this case results in the same intensity profile. In general, however, this may not be true for all cases.

In terms of applicability in more complex simulations that include tracing and multiple reflections, it is important to think about how to practically implement beam-sample interaction simulation. It would be ideal to obtain an analytical relation that describes the spatial and energy distribution of signal electrons for each condition. However, we do not have this relation and it is not easy to obtain. It would be necessary to perform a fit of the 3D solids and try to find the dependence between the parameters for more cases. However, the question arises again of how to find this dependence and how many variables to examine. When we have a database of trajectories, some can be randomly selected from the list and thereby preserve the probability distribution. For example, if the generation of a high-energy electron is more likely, then we are also more likely to select the higher-energy electron from our list because there are more of them. The gaps between the simulation points were solved by choosing with some probability from one list and with some probability from the other. For example, if we have created a simulations for sample tilt angles of 2°and 4°, but we need to find out which electrons are produced at a tilt of 3°, then with a 50 % probability we select an electron from the list for 2°degrees and with a 50 % probability from the list for 4°. In the end, this approach proves to be the most practical.
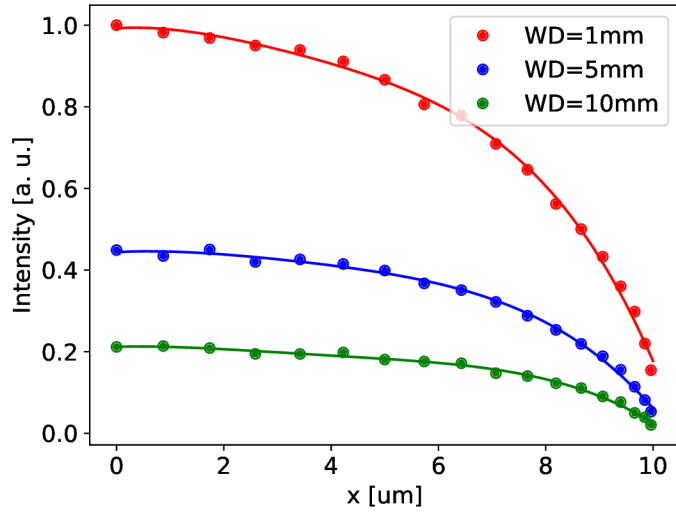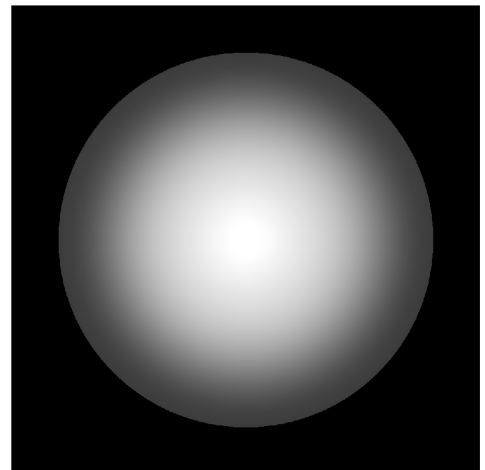
(a) Standard intensity profile.
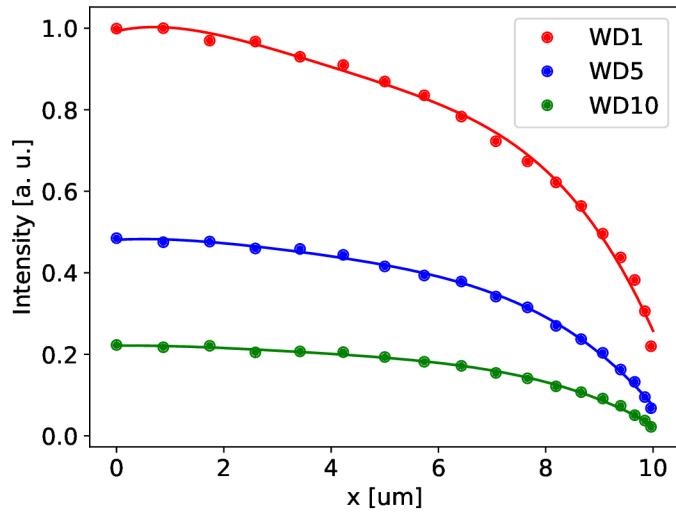
(b) Optiplan intensity profile.
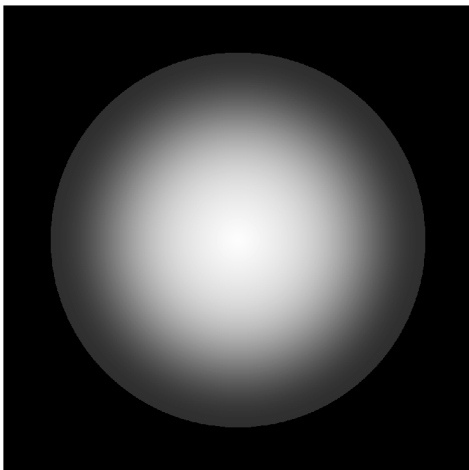
(c) Standard image simulation.

(d) Optiplan image simulation.

Figure 4.9: Intensity profile of a tin ball simulated by Casino software and filtered by acceptance diagrams. Visualized for 1 mm, 5 mm and 10 mm WDs. Based on polynomial fit, the image simulation was generated for WD 1 mm.
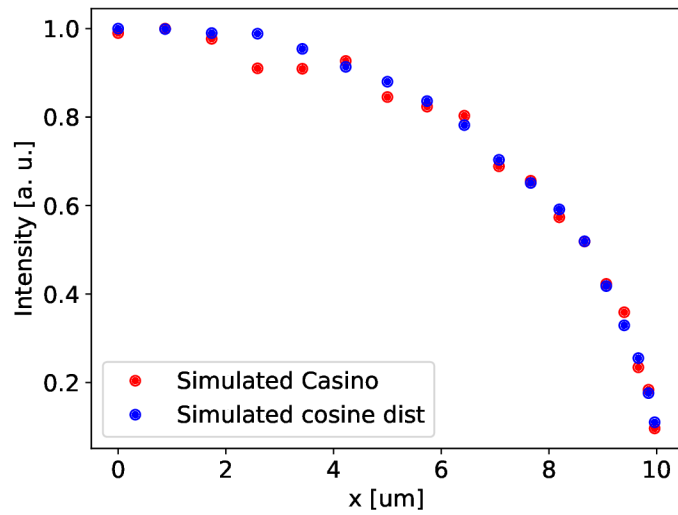
Figure 4.10: Comparison of intensity profiles of a tin ball simulated by Casino software and simplified tilted cosine distribution as it is described in section 4.2. The simulation data was processed via T1 acceptance at 10 mm WD and Standard usecase.

Chapter 5

Experiments

I performed measurements aiming at experimental determination of material and topographic contrast of BSE in a SEM. I was given access to an Apreo scanning electron microscope at Thermo Fisher Scientific Brno, s.r.o.

5.1   Material contrast

To describe material contrast, the measurements were performed on a flat set of single element samples shown in Figure 5.2. The set containing 8 single-element samples was manufactured by MAC company and the aluminium stub has a diameter of 25 mm. The serial number is 14271. The measurements were made with an accelerating voltage of 10 kV and detection was provided by T1 detector. The probe current was 1.08 nA. First, I set on the lowest WD brightness so that when the beam is blanked, the image is black, then I set the contrast level on the element with the highest atomic number so that it is closest to white in the image. This gave me the largest possible range in which I could measure the drop in intensity. I gradually took pictures of the other elements and watched the decrease in intensity. I selected an area without defects and cracks from the images and calculated the average gray level value from it. Then I switched to a higher WD where additional drop in intensity occurred and I took images of all the elements again. I repeated the procedure for WD 5 to 10 mm with a step of 1 mm. Illustration of this decrease in intensity are in Figure 5.3, where the individual WDs are distinguished by color and the points are fitted by the curve described by Equation 3.6 multiplied by a fitting coefficient. I set the intensity in the graph so that the most intense point has a value of 1. With higher WDs, it is not entirely clear whether the curve fits the measured points, so I included a few extra elements in the next measurement, especially gold, which is heavier, so the curve contains a larger range.

I performed the measurements with Ti, Ni, Mo and Au on different probe currents, but then I normalized the intensity level so that it sat at the level corresponding to the curve described by Equation 3.6. The result is graphically depicted in Figure 5.4. The dashed line indicates Equation 3.6 and we can see that it fits well with the measurement. Spot 11 corresponded to 736 pA, spot 12 1.45 nA and spot 13 was 3.15 nA. It is a verification that the shape of the curve is the same for different currents.

With this, we have definitively verified Equation 3.6. We are able to predict the intensity difference between two bordering elements for all combinations.

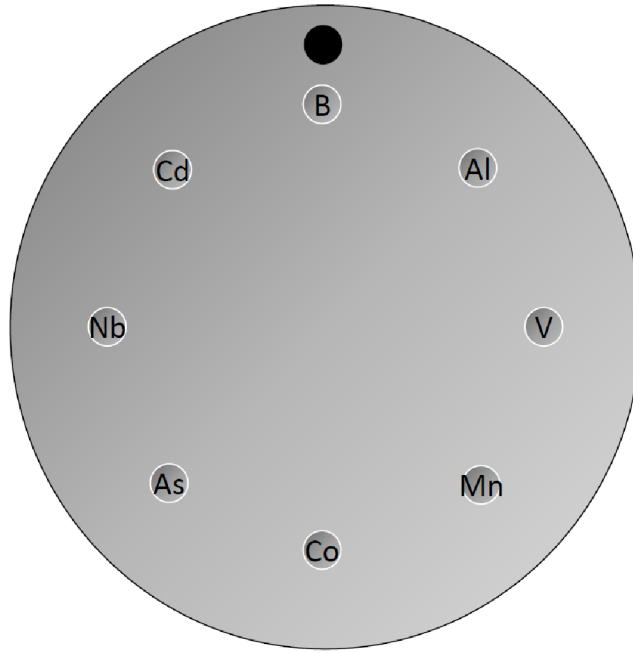Figure 5.1: Apreo scanning electron microscope on which the measurements were performed [54].

Figure 5.2: Single element flat sample standard with a diameter of 25 mm containing 8 single-element samples manufactured by MAC company. The serial number is 14271.
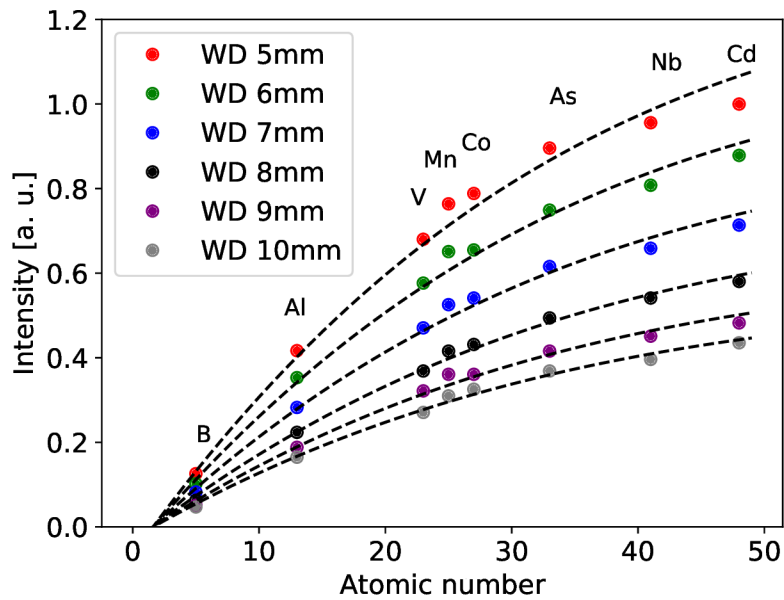

Figure 5.3: Measurement of BSE coeficient for multiple WDs and different materials. Dots denote the experiment data, the dashed lines the respective fits.
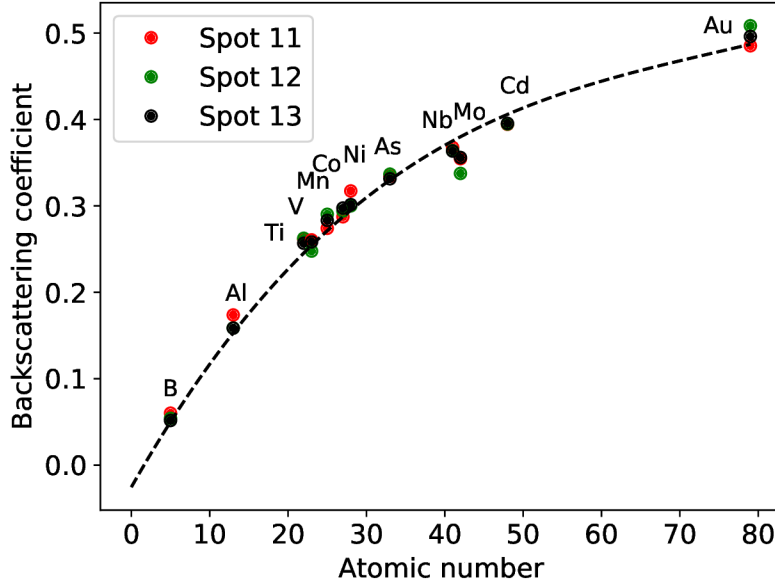
Figure 5.4: Measurement of BSE coeficient for multiple spot sizes with addition of Ti, Ni, Mo and Au sample.

5.2 Topographic contrast

To investigate the topographical contrast, I used a sample of tin balls as depicted in Figure 5.5. I performed the measurements again at landing energy 10 keV and with the T1 detector. The purpose was to obtain the experimental intensity profile of a tin ball. Measurements were made on WD 1 mm, 5 mm and 10 mm using Standard and Optiplan usecases corresponding to the carried out simulations. The resulting intensity profile from the T1 detector measurement is shown in Figure 5.6. As it is demonstrated in Figure 5.7, I got the intensity profile by selecting a ball, transforming it into polar coordinates and integrating over the angle, so I received dependence only on the radius. That way I got a smoother curve and better statistics than if I had taken some random line from the center to the edge. Standard was measured with 1.04 nA current, Optiplan on 607 pA. Before measurement, I adjusted the brightness by blanking the beam and setting the level to black, and with the parameter of contrast gain I regulated the range so that the center of the sphere was not saturated. The spheres evaluated were of different sizes, so I set the scale in the graph to a radius of 10 μm so that the results were comparable.

Later, there was another measurement performed on CBS detector which was used for comparison because it utilizes direct detection in contrast to the T1 detector. The position of the detector was a bit restrictive with respect to possible WDs, so I measured on WD 10 mm. The current was 568 pA.

To further simplify the situation, I took a flat sample of cadmium because it is close to tin in atomic number and tilted it with a step of 5°. The measurement was performed on T1 at 10 mm WD which allowed for sample tilting, the current was 2.05 nA. The result is shown in Figure 5.9. For subplot b), I transferred the dependence on angle to
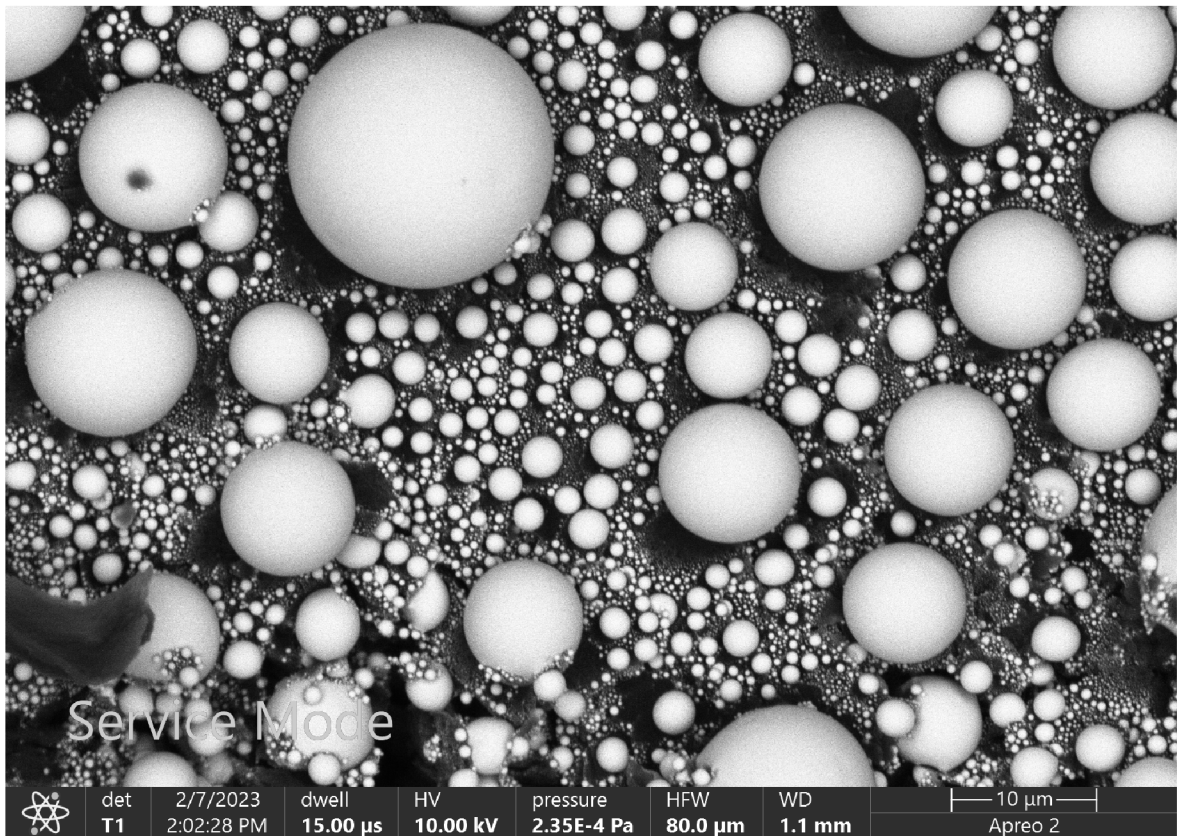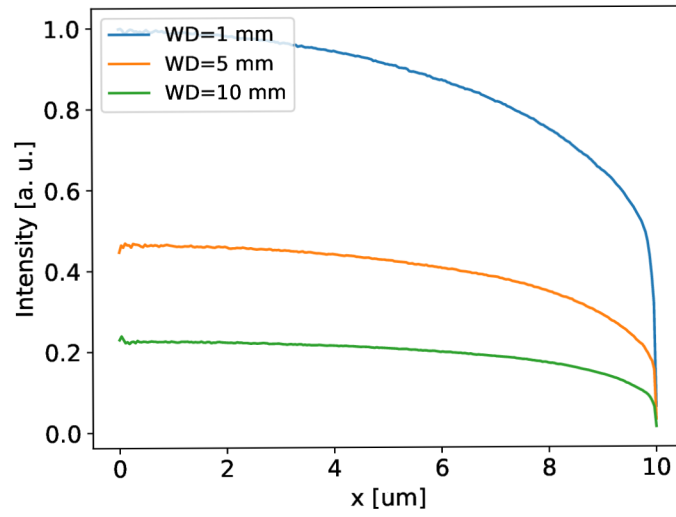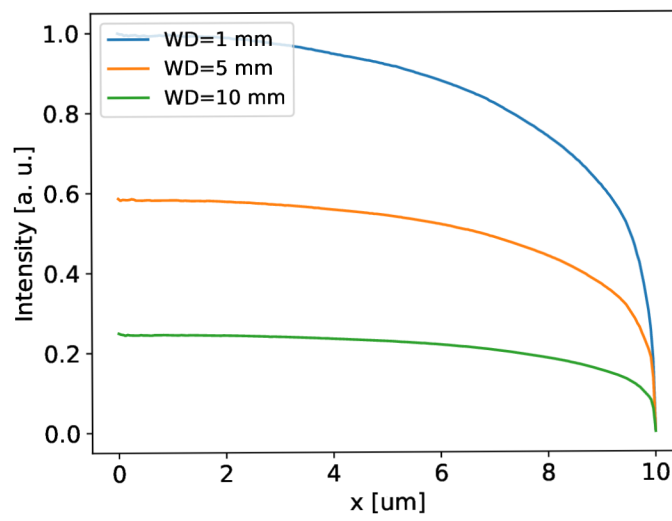
Figure 5.5: Typical appearance of a sample of tin balls when measured with a T1 detector in Standard usecase.
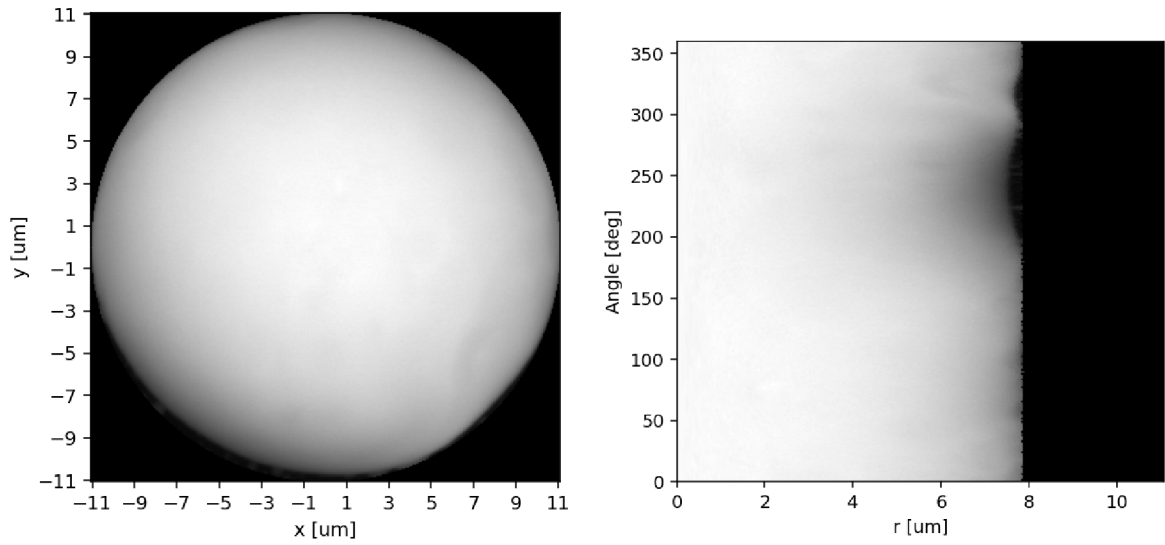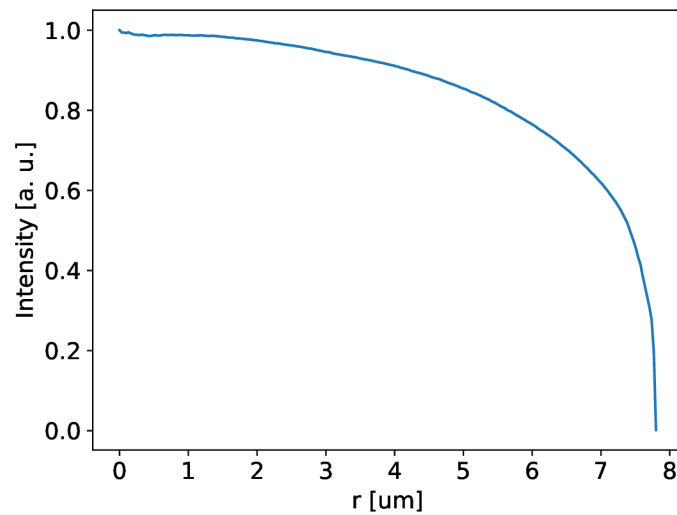
(a)

(b)

Figure 5.6: Intensity profiles of measured tin balls for a) Standard and b) Optiplan usecase.

(a)

(b)

(c)

Figure 5.7: Demonstration of a workflow of displaying an intensity profile of a tin ball image. a) Selected tin ball, the area around the ball is removed by applying a circular mask. b) Image converted to polar coordinates. c) Intensity profile after integration over angle and normalization.
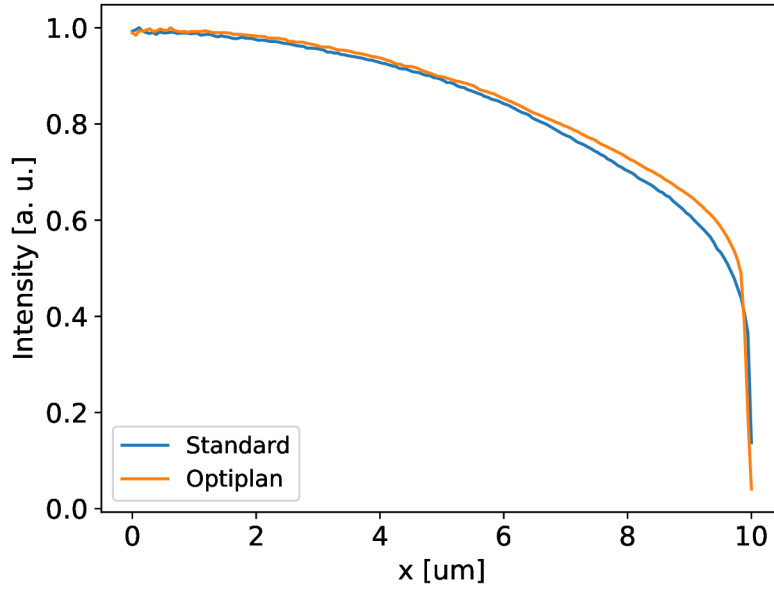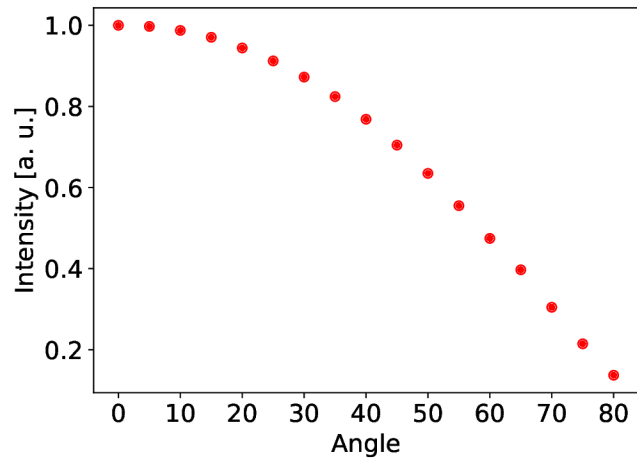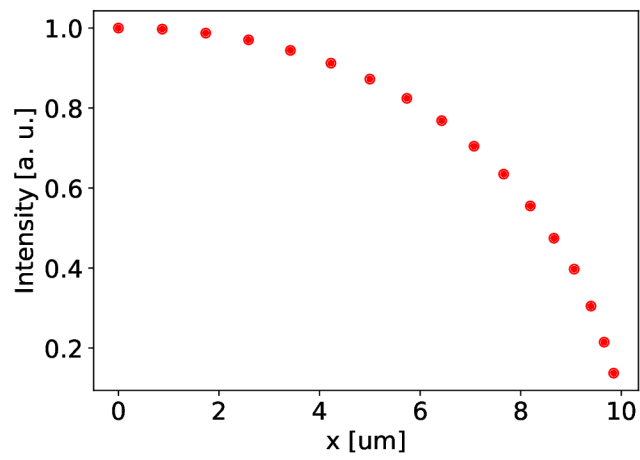
Figure 5.8: Intensity profiles of measured tin balls on CBS detector.

dependence on radius on a ball. We can see that the decrease in intensity is again more gradual than with direct measurement on the ball. Comparison with the simulation can be found in the next chapter.

(a)

(b)

Figure 5.9: Cd tilt measurement results. a) Angle dependence, b) transformed to a dependence of radius on a ball.

Chapter 6

Comparison of simulations and experiments

A comparison of the simulation of the material contrast with the measurement and with the equation Equation 3.6 can be found in Figure 6.1. Simulated points were generated in Casino using 100 000 trajectories, the equation Equation 3.6 is depicted by dashed line. Uncertainties of the measured points were determined by the deviation of the gray level from equally sized areas on the sample. There were a lot of cracks on the samples of some elements and therefore the uncertainty is greater. In general, however, we can see that the measurements, simulations and theoretical curve fit well together.

In Figure 6.2, we see a comparison of the simulation from Figure 4.9 and the measurement from Figure 5.6. Measurement is depicted by continuous line and simulation by points. Measurements and simulations are made with landing energy 10 keV, detection by T1, WD 1 mm, 5 mm and 10 mm, Standard and Optiplan usecases. We can see that the measurement and simulation differ in the shape of the curve and, in the case of Optiplan, in the drop in gray level when going from WD 1 mm to 5 mm. For simplicity, I will focus on the Standard usecase and try to investigate why in this case the measurement does not match the simulation.

As the first possible explanation, I included the reflection from the pole piece in the simulation. The pole piece is a permalloy part that extends below the T1 detector. There is also an aluminium ring placed inside the pole piece that sits below T1 detector. From its geometry, I calculated the accepted angles for a given WD and found out which electrons hit it using the same procedure as when determining the acceptance of the detector. I added this acceptance to the acceptance of the T1 detector and got the orange points in Figure 6.3. At first glance it seems that this explained the discrepancy, but here I assumed that everything that hits the pole piece will be reflected at T1, which in reality would not happen, since the coefficient of backscattering of aluminum is around 0.164 and for combination of nickel 48 % and iron 52 %, which makes up permalloy, it is 0.231. T1 would also occupy only a limited angle range. In addition, the effect of reflection is less pronounced with WD because the range of received angles is smaller and smaller, which we see at WD 10 mm in the graph that the curve with the reflection lies on the curve without it. Therefore, this phenomenon cannot explain the slower intensity decrease near the center and the sharp decrease at the edge of the ball in the measurement compared to the simulation. I also tried to include in the
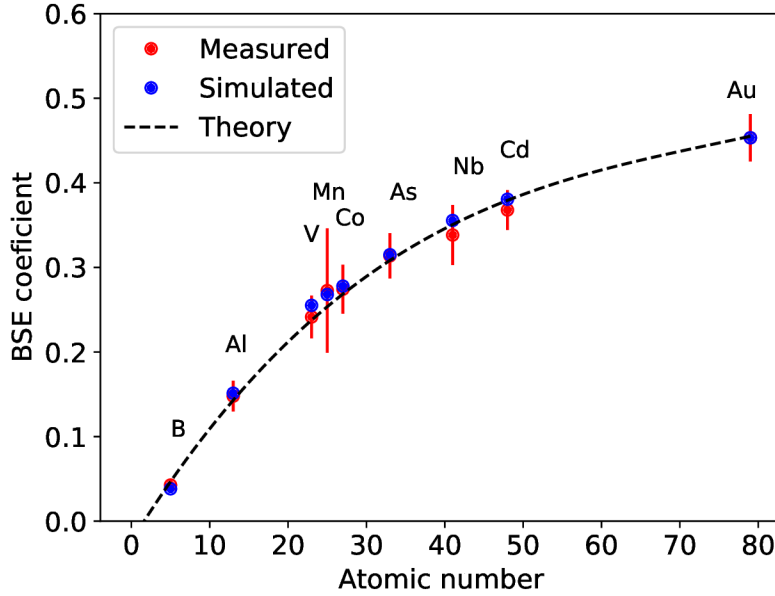
Figure 6.1: Measurement of BSE coeficient compared to simulation results obtained from Casino and equation Equation 3.6.

simulation the absorption from the gap between the pole piece and T1, because T1 has part of the active surface from the inside as well. However, this approach did not lead anywhere, because it increased the intensity more in the center and not near the edge. I also included the reflection from the sample itself, so I selected electrons pointing downwards, which I again defined by certain angles. But the tendency in the image in that case would be such that the edge would be lighter than the center, which does not happen with BSE detection. Next, by tilting the sample with tin balls, I verified that they are really round. I watched a particular larger ball and tilted the sample. However, it retained its round shape.

In Figure 6.4, we can see a comparison of one simulation and two measurements. In this case, measurements and simulation were performed on WD 10 mm again on the T1 detector. The red points represent the simulated intensity profile from Casino where I simulated a tilt of a tin surface. The green curve is the measured profile of the real tin ball. For comparison, there is a measurement with tilted Cd surface. An experiment on a flat and tilted surface was performed. Since I have not a Tin flat surface sample at my disposal, I used a present Cadmium flat specimen. Atomic number of Cd is 48 which is close to Sn that has 50. The maximums were normalized to 1. In the figure, it is visible that there is an agreement between simulation and measurement of the tilted Cd surface but not with the tin ball intensity profile measurement.

The next step to explain the difference in the intensity profiles was measuring the response of T1 detector. I used the apertures to set different current levels and used a flat metal surface as a sample. For each current, I set the brightness so that when the beam is blanked, we get a black level on the screen. Then I adjusted the contrast so that the gray level on the sample was in the middle of the range. The contrast value that needs to be set is related to the response. The dependence of the contrast
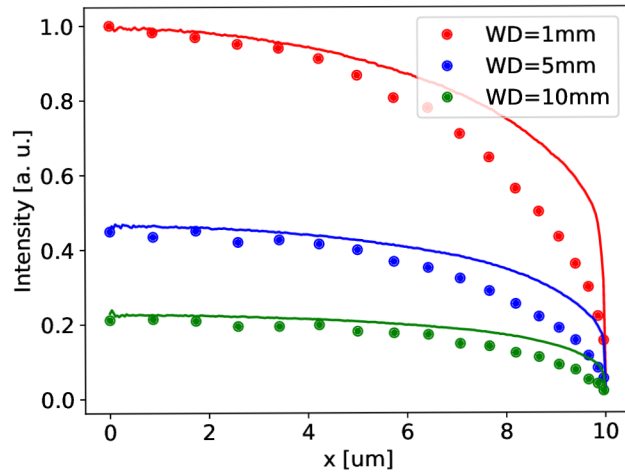
(a)
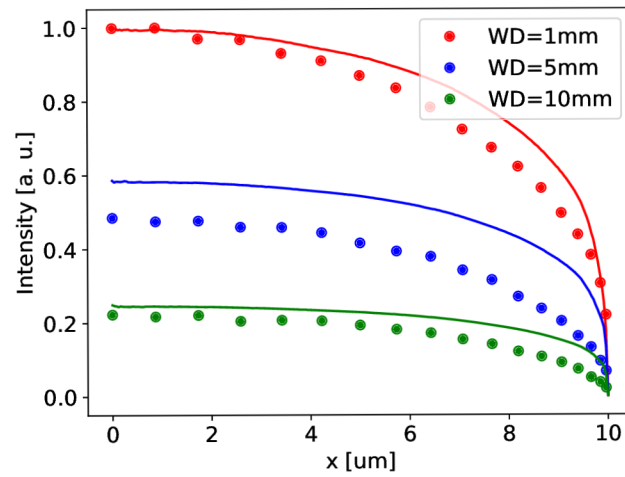
(b)

Figure 6.2: Comparisons of measured (continuous line) and simulated (points) intensity profile of a tin ball. a) Standard and b) Optiplan usecase. Landing energy 10 keV, detector T1, WD 1 mm, 5 mm and 10 mm.
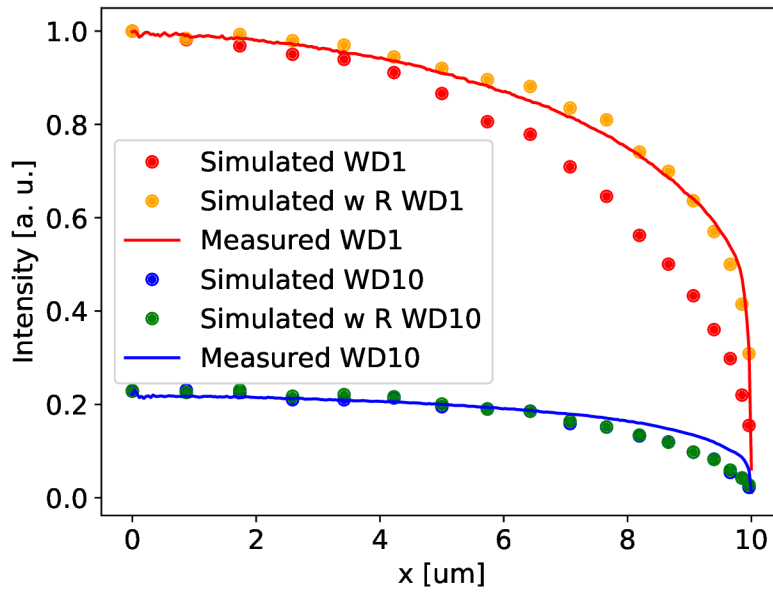
Figure 6.3: Comparison of measured and simulated tin ball intensity profile with reflection from pole piece (w R) for 1 mm and 10 mm WD. Measured on T1.
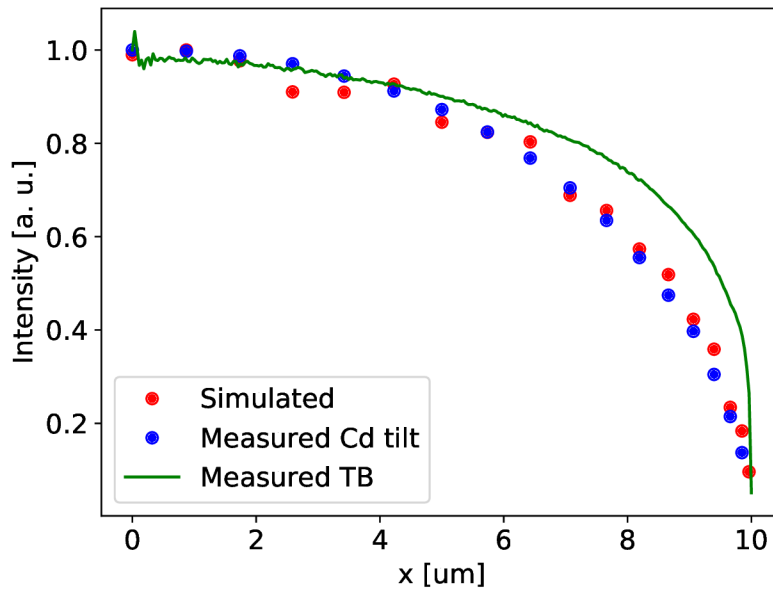

Figure 6.4: Results from Casino simulation compared to measurement of decrease in intensity on tilted flat Cd sample and intensity profile of a tin ball. Measured on WD 10 mm, T1 detector.
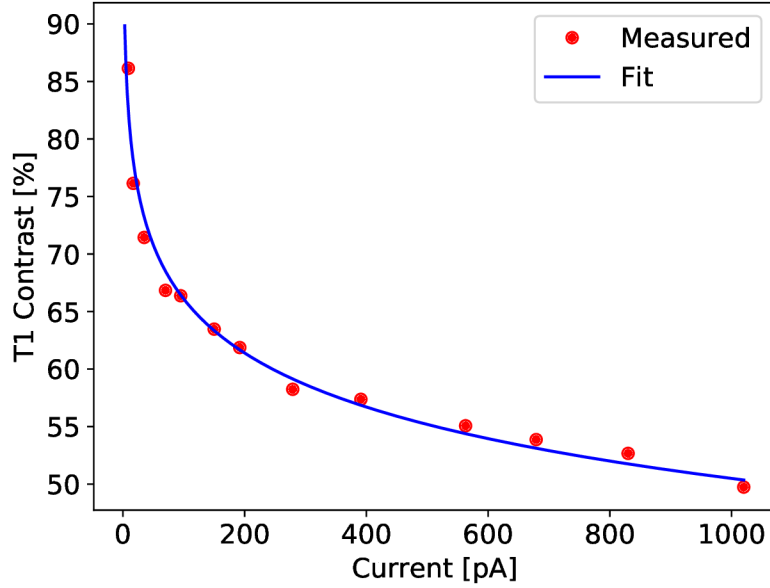
Figure 6.5: Measured inverse response of T1 detector.

on the current is shown in Figure 6.5. I fitted the measured points with a function in the shape $A + B \log(x)$, where A is 97 ± 2 and B is -6.8 ± 0.3. This dependence is not directly the response, rather it is the inverse function of the response described by Equation 2.6. However, during the measurements I present here, the current was in the region above 200 pA, so we stayed in the relatively linear part of the curve.

Measurements on the CBS detector were another way to verify whether the effect on the tin ball is caused by the detection and response of the T1 detector. As it employs a direct detection, it has a different response and can potentially produce a different characteristic than the T1. The result of the measurement and comparison with the simulation can be seen in Figure 6.6. We can see that the problem with the curve bulging towards the edge of the ball persists on this detector as well. On CBS, it was not possible to measure at a much smaller WD than 10 mm, so I measured at 10 mm, noting that even the drop in intensity when moving to a higher WD does not correspond to the simulation. The simulated blue points are actually below the measured blue curve. Thus, we see that the discrepancy with the simulation is not due to the scintillator and mechanisms associated with it.

In the simulation, we did not take into account the influence of the interaction volume, which might, however, be significant and could explain why there is a difference in the measurement of the tilt of the flat sample and the measurement directly on the ball. Interaction volume for Sn simulated in Casino v2 is depicted in Figure 6.7. We can see that the area from which the BSE originate comes close to $800x800nm^2$. According to Equation 3.1, the radius of a sphere that should contain 95% trajectories for Sn primary energy 10 kV is 650 nm. As the sample tilts, the interaction volume loses its rotation symmetry. However, if there is a ball defined as a sample in Casino and a scan is performed from the center to the edge, then the intensity profile does not differ in any way from the intensity profile obtained by gradually tilting a flat surface. Casino
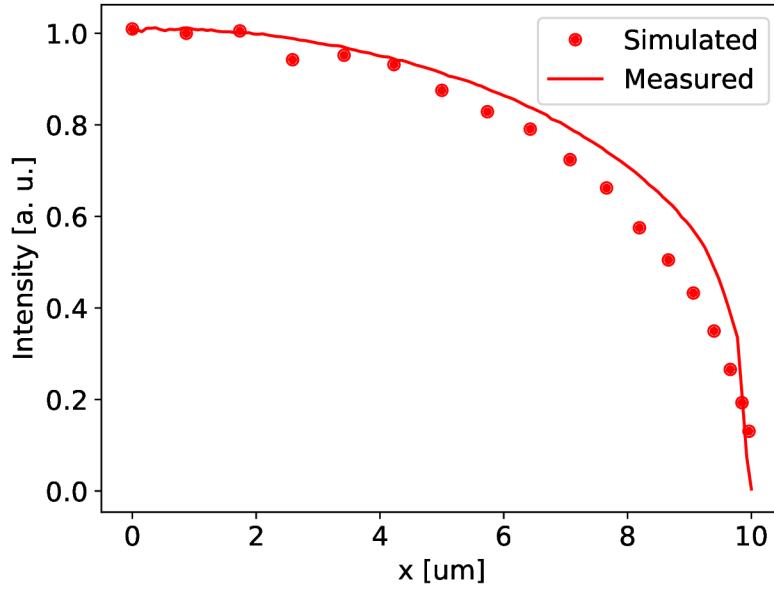
Figure 6.6: Simulation and measurement of tin balls on CBS detector, WD 10 mm.

inherently takes interaction volume into account so this shows that this explanation may not be valid either.

The result is that the agreement of measurements, simulations and theory was achieved in the case of material contrast. In the case of topographical contrast, I obtained agreement with simulation only with one type of measurement, namely by tilting a flat cadmium surface and measuring gray level drop on the images. When evaluating measurements on tin balls, I did not find an agreement with the simulation, which would be consistent across different conditions and well-founded physically. Apparently there is a factor that has not been determined and taken into account.
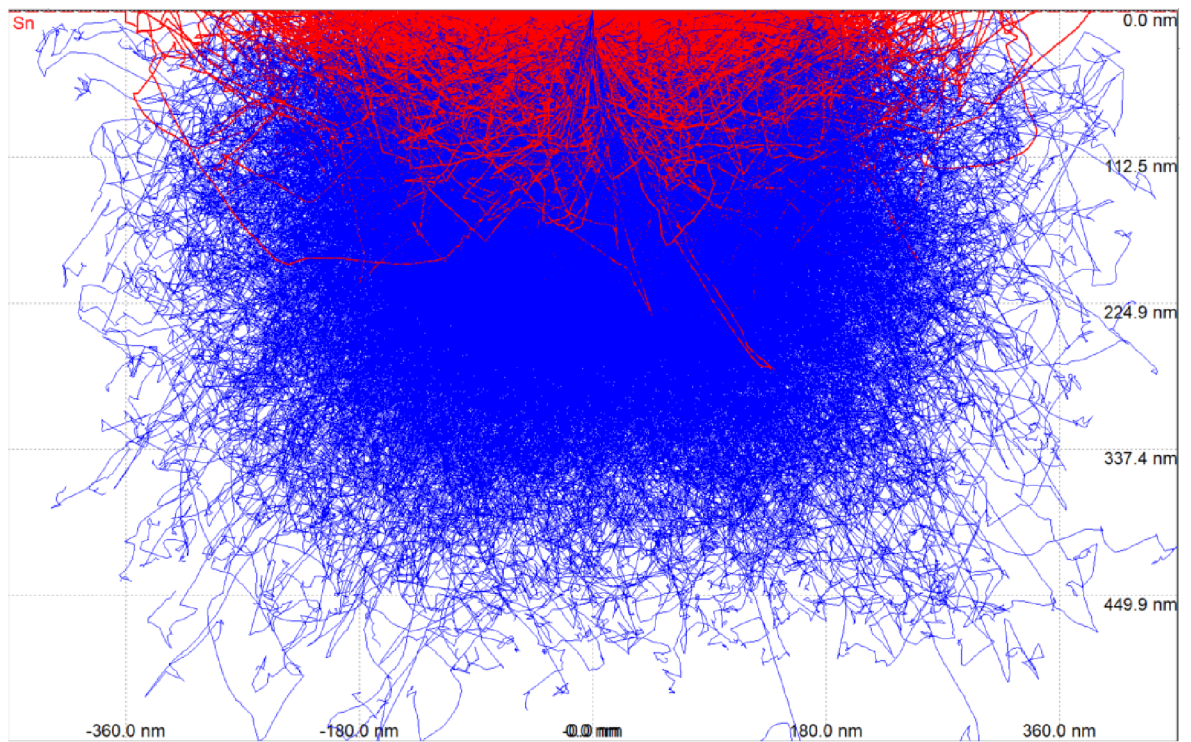
(a)
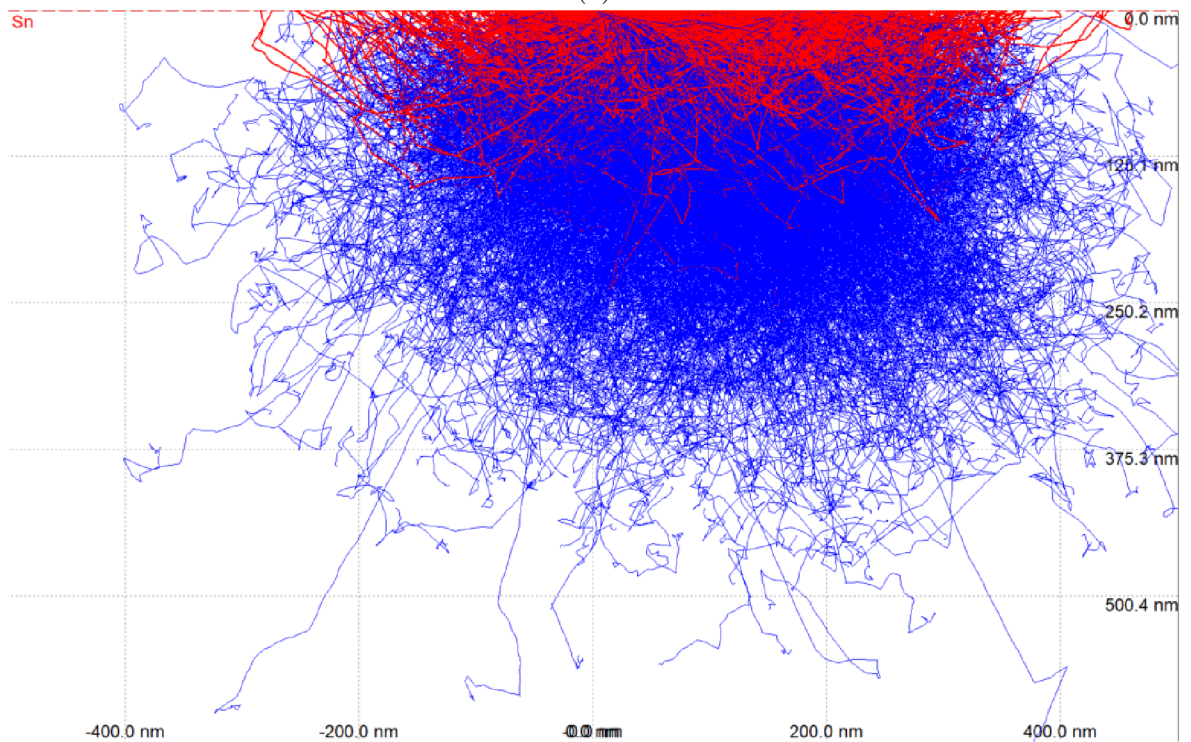
(b)

Figure 6.7: Simulated interaction volume for Sn with primary energy 10 keV for a) perpendicular impact and b) tilt 80°. Simulation was made in Casino v2 with 10 000 primary electrons. Red lines depict trajectories of BSE, blue are absorbed electrons.

Conclusions

The purpose of this research is to explain how contrast is produced in a scanning electron microscope and to replicate images using an understanding of the settings of the microscope. I created simulations in the Casino program, which I further filtered by acceptance of the detector based on the column model and performed measurements to compare with these simulations.

In chapter 1, I go into basics of electromagnetic field description (section 1.1) and its connection to electron trajectory calculation (section 1.2). I describe the optics of the scanning electron microscope in chapter 2. The electron source, the electromagnetic lens system, and optical aberrations are covered in section 2.1 and section 2.2 there is an analysis of the optics of signal electrons, which includes the types of the detectors, the field that affects the signal electrons and the characteristics of the detectors such as their position, efficiency and response. The output of the analysis is the angular and energy acceptance of the detectors. The chain of post-processing is described in section 2.5 and mechanisms of image formation in section 2.4. In chapter 3, there is an overview of the signals we get when the beam interacts with the sample and description of the mechanisms of their formation. Essential concepts such as interaction volume and basic characteristics of signal electrons such as their energy and spatial distribution are explained there. The most important for the description of the material contrast is Equation 3.6 that contains the dependence of the backscattering coefficient on the atomic number. Spatial distribution and the dependence of the backscattering coefficient on the surface tilt are important for topographic contrast.

In chapter 4, there are two models of backscattered electron emissivity. The section 4.1 discusses analytical and numerical methods in general. In section 4.2, I present a simplified model using tilted cosine distribution and show a simulation of what would an intensity profile of a ball look like in Figure 4.2. In section 4.3, I show how the simulation software Casino works, partly how it can be controlled and I also show the resulting spatial distribution of BSE in a form of 3D histogram Figure 4.6 which I designed in Python. It shows that for heavier elements the distribution sticks more closely to cosine with tilt of the sample, and for lighter ones the reflection effect is more pronounced. I also mention the Nebula software that I used for comparison with Casino. The energy spectrum of Nebula data is more accurate but it does not show much difference in the resulting simulated image. A concrete example of acceptance diagrams can be found in section 4.4 together with resulting intensity profiles of a tin ball Figure 4.9 and simulated images of a tin ball I made in Python. An interesting observation is that when we compare the intensity from the simulation done in Casino with the intensity created by the tilted cosine distribution with the same number of BSE for each tilt, we do not see a difference. This can be used as a justification for using a simplified model. The measurements I made on the Apreo SEM at the Thermo

Fisher Scientific company are presented in chapter 5. Experiments concerning material contrast are described in section 5.1. They basically consist of measuring the decrease in intensity when we go from a sample with a higher atomic number to a sample with a smaller one. The section 5.2 covers the measurement of topographic contrast. There we find the measurement of tin balls under different conditions and the measurement of the decrease in intensity when tilting a flat surface of cadmium.

The chapter 6 is crucial because there is comparison between simulation and measurement. It turned out that in the case of material contrast, Equation 3.6, simulated points in Casino and measurements fit together in Figure 6.1. In the case of topographical contrast, there was a discrepancy between the intensity course on the tin ball and the simulation, and in some optical modes the decrease in intensity when moving to a higher working distance did not fit. As a first theory, the effect of reflection from the pole piece was tested, but it was only manifested at low working distances and in reality it would be manifested only to a very small extent. We obtained a good agreement only in Figure 6.4, which shows the comparison of the simulation with the cadmium tilt measurement. However, the course of the intensity on the tin ball still does not correspond to this curve. The response of the T1 detector was measured and a measurement was also performed on tin balls with a CBS detector. The CBS detector works on the principle of direct detection. The simulation courses do not match the measurement in the same way as measurements performed on T1. Apparently there is a factor that has not been determined and taken into account.

My work can advance the understanding of contrast formation a step further and contribute to the discussion about the practicality and functionality of using different models for BSE emission. The future outlook consists in including more effects and describing the emission of secondary electrons. The models need to be extended to more measurement conditions to be able to simulate the image for a wide range of settings. The future of simulating images and creating a digital twin of a microscope is promising and offers many uses.

References

[1]   H. Gunther Rudenberg and Paul G. Rudenberg. "Origin and background of the invention of the electron microscope". In: *Advances in Imaging and Electron Physics* (2010), pp. 207–286. DOI: `10.1016/s1076-5670(10)60006-7`.

[2]   Christine G. Golding et al. "The Scanning Electron Microscope in microbiology and diagnosis of infectious disease". In: *Scientific Reports* 6.1 (2016). DOI: `10.1038/srep26516`.

[3]   Ronald E. Gordon. "Electron microscopy: A brief history and review of Current Clinical Application". In: *Histopathology* (2014), pp. 119–135. DOI: `10.1007/978-1-4939-1050-2_7`.

[4]   Alexey S. Kashin and Valentine P. Ananikov. "Monitoring chemical reactions in liquid media using electron microscopy". In: *Nature Reviews Chemistry* 3.11 (2019), pp. 624–637. DOI: `10.1038/s41570-019-0133-z`.

[5]   Peng Zhang et al. "Industrial applications of electron microscopy: A shared laboratory perspective". In: *Microscopy and Microanalysis* 25.S2 (2019), pp. 690–691. DOI: `10.1017/s1431927619004185`.

[6]   ROBIN C. VALENTINE. "Contrast in the electron microscope image". In: *Nature* 181.4612 (1958), pp. 832–833. DOI: `10.1038/181832b0`.

[7]   Dirk van Dyck Amelinckx. *Electron Microscopy: Principles and Fundamentals.* Wiley, 2008.

[8]   ANWAR UL-HAMID. *Beginners' Guide to Scanning Electron Microscopy.* Springer, 2019.

[9]   Ludwig Reimer. *Scanning electron microscopy: Physics of image formation and microanalysis.* Springer, 2010.

[10] *Scanning electron microscopy: Electrons in SEM: Thermo Fisher Scientific.* URL: `https://www.thermofisher.com/de/de/home/materials-science/learning-center/applications/sem-electrons.html`.

[11] Inspiration Education Limited, 2021.

[12] Leonard Susskind and Art Friedman. *Special relativity and classical field theory: The theoretical minimum.* Basic Books, 2019.

[13] Anwar Ul-Hamid. *A beginners' guide to Scanning Electron Microscopy.* Springer, 2018.

[14] Isaac Newton and ANDREW MOTTE. *Newton's Principia: The mathematical principles of natural philosophy.* BLURB, 2018.

[15] Tomáš Neugebauer. "Advanced numerical techniques for ordinary defferential equation system." diplomathesis. Brno University of Technology, 2023.

[16] *CST Studio Suite 3D EM Simulation and Analysis Software*. URL: https://www.3ds.com/products-services/simulia/products/cst-studio-suite/.

[17] Lencová and Zlámal. *EOD - Electron Optical Design software, electron and ion optics*. July 2022. URL: https://www.lencova.com/index.php/about-eod..

[18] Weilie Zhou et al. "Fundamentals of Scanning Electron Microscopy (SEM)". In: *Scanning Microscopy for Nanotechnology* (2006), pp. 1–40. DOI: 10.1007/978-0-387-39620-0_1.

[19] Alex Ilitchev. *How do you make an electron beam?* July 2022. URL: https://www.thermofisher.com/blog/materials/electron-source-fundamentals/.

[20] Peter W. Hawkes. *Magnetic electron lenses*. Springer, 1982.

[21] Anjam Khursheed. *Scanning electron microscope optics and spectrometers*. World Scientific, 2011.

[22] Monika Dovičinová. "Photonic detectors as quantum random number generators." Bachelor's thesis. Palacký University Olomouc, 2021.

[23] L. Neri et al. "Dead time of single photon avalanche diodes". In: *Nuclear Physics B - Proceedings Supplements* 215.1 (2011), pp. 291–293. DOI: 10.1016/j.nuclphysbps.2011.04.034.

[24] Abdul Waris Ziarkash et al. "Comparative study of afterpulsing behavior and models in single photon counting avalanche photo diode detectors". In: *Scientific Reports* 8.1 (2018). DOI: 10.1038/s41598-018-23398-z.

[25] Michael Hofbauer, Bernhard Steindl, and Horst Zimmermann. "Temperature dependence of dark count rate and after pulsing of a single-photon avalanche diode with an integrated active quenching circuit in 0.35M CMOS". In: *Journal of Sensors* 2018 (2018), pp. 1–7. DOI: 10.1155/2018/9585931.

[26] Feb. 2020. URL: http://www.teamwavelength.com/maintenance/photodiode-basics/.

[27] Natasha Erdman, David C. Bell, and Rudolf Reichelt. "Scanning Electron Microscopy". In: *Springer Handbook of Microscopy*. Ed. by Peter W. Hawkes and John C. H. Spence. Cham: Springer International Publishing, 2019, pp. 229–318. ISBN: 978-3-030-00069-1. DOI: 10.1007/978-3-030-00069-1_5. URL: https://doi.org/10.1007/978-3-030-00069-1_5.

[28] Libor Novák. "Methods for quantification of detection channel for secondary electrons in scanning electron microscope." PhD thesis. Masaryk University, 2011.

[29] G. KNOP and W. PAUL. "Interaction of electrons and -particles with matter". In: *Alpha-, Beta- and Gamma-Ray Spectroscopy* (1968), pp. 1–36. DOI: 10.1016/b978-0-7204-0083-0.50006-7.

[30] T J Shaffner and R D Veld. "'charging' effects in the scanning electron microscope". In: *Journal of Physics E: Scientific Instruments* 4.9 (1971), pp. 633–637. DOI: 10.1088/0022-3735/4/9/002.

[31] Amin I. Kassis. "The Amazing World of Auger electrons". In: *International Journal of Radiation Biology* 80.11-12 (2004), pp. 789–803. DOI: 10.1080/09553000400017663.

[32] Joseph I. Goldstein et al. *Scanning electron microscopy and X-ray microanalysis*. Springer, 2018.

[33] John F. Moulder and Jill Chastain. *Handbook of X-ray Photoelectron Spectroscopy: A reference book of standard spectra for identification and interpretation of XPS Data*. Perkin-Elmer Corporations, Physical Electronics Division, 1992.

[34] David C. Bell and Natasha Erdam. *Low voltage electron microscopy: Principles and applications*. Wiley, 2013.

[35] Ono S. Kanaya K. "Interaction of electron beam with the target in scanning electron microscope". In: 1984, pp. 69–98.

[36] Kurt F Heinrich. In: *Scanning electron probe microanalysis.* (1965). DOI: 10.6028/nbs.tn.278.

[37] W. Reuter. "Electron backscattering as a function of atomic number." In: *University of Tokyo Press* (1972), pp. 121–122.

[38] Eli Peli. "Contrast in complex images". In: *Journal of the Optical Society of America A* 7.10 (1990), p. 2032. DOI: 10.1364/josaa.7.002032.

[39] Johann Heinrich Lambert. *Photometria sive de mensura et gradibus luminis, colorum et umbrae*. E. Klett, 1760.

[40] F. Arnal, P. Verdier, and P. D. Vinsensini. "Coefficient de retrodiffusion dans de cas d'electrons monocinetiques arrivant sur la cible sous une incidence oblique." In: *Compt. rend. Acad. Sci.* (1969), pp. 268–269.

[41] E H Darlington and V E Cosslett. "Backscattering of 0.5-10 kev electrons from solid targets". In: *Journal of Physics D: Applied Physics* 5.11 (1972), pp. 1969–1981. DOI: 10.1088/0022-3727/5/11/305.

[42] Eugene J. Segre. *Experimental nuclear physics*. Wiley and Sons, 1953.

[43] F. A. Lukiyanov, E. I. Rau, and R. A. Sennov. "Depth range of primary electrons, electron beam broadening, and spatial resolution in electron-beam studies". In: *Bulletin of the Russian Academy of Sciences: Physics* 73.4 (2009), pp. 441–449. DOI: 10.3103/s1062873809040029.

[44] ReCOm. *Analytical And Simulation Models*. Feb. 2012. URL: https://www.recomedu.net/analytical-and-simulation-models/.

[45] Dirk P. Kroese et al. "Why the monte Carlo method is so important today". In: *WIREs Computational Statistics* 6.6 (2014), pp. 386–392. DOI: 10.1002/wics.1314.

[46] URL: https://www.gegi.usherbrooke.ca/casino/.

[47] Hendrix Demers et al. "Three-dimensional electron microscopy simulation with the casino monte carlo software". In: *Scanning* 33.3 (2011), pp. 135–146. DOI: 10.1002/sca.20262.

[48] Khronos Group. *The industry's foundation for High Performance Graphics*. URL: http://www.opengl.org/.

[49] Tomas Möller. "A fast triangle-triangle intersection test". In: *Journal of Graphics Tools* 2.2 (1997), pp. 25–30. DOI: 10.1080/10867651.1997.10487472.

[50] Francesc Salvat, Aleksander Jablonski, and Cedric J. Powell. "Elsepa—dirac partial-wave calculation of elastic scattering of electrons and positrons by atoms, positive ions and molecules". In: *Computer Physics Communications* 165.2 (2005), pp. 157–190. DOI: 10.1016/j.cpc.2004.09.006.

[51]   Masatoshi Kotera et al. "A simulation of electron scattering in metals and its application for scanning electron microscopy". In: *Proceedings, annual meeting, Electron Microscopy Society of America* 48.1 (1990), pp. 420–421. DOI: 10.1017/s0424820100180859.

[52]   J Lowney and Egon Marx. *User's Manual for the Program MONEL-I: Monte Carlo Simulation of SEM Signals for Linewidth Metrology*. en. 1995-01-01 00:01:00 1995.

[53]   L. van Kessel and C.W. Hagen. "Nebula: Monte Carlo Simulator of electron–matter interaction". In: *SoftwareX* 12 (2020), p. 100605. DOI: 10.1016/j.softx.2020.100605.

[54]   *Thermo Fisher Scientific accelerates nanometer-scale research with Apreo 2*. Aug. 2020. URL: https://www.industrialautomationindia.in/newsitm/10410/Thermo-Fisher-Scientific-accelerates-nanometer-scale-research-with-Apreo-2/news.